

HyperAIRI: a plug-and-play algorithm for precise hyperspectral image reconstruction in radio interferometry

Chao Tang,^{1,2} Arwa Dabbech,¹ Adrian Jackson,² and Yves Wiaux^{1*}

¹*Institute of Sensors, Signal, and Systems, Heriot-Watt University, Currie, Edinburgh EH14 4AS, UK*

²*EPCC, University of Edinburgh, 47 Potterrow, Edinburgh EH8 9BT, UK*

Accepted XXX. Received YYY; in original form ZZZ

ABSTRACT

The next-generation radio-interferometric (RI) telescopes require imaging algorithms capable of forming high-resolution high-dynamic-range images from large data volumes spanning wide frequency bands. Recently, AIRI, a plug-and-play (PnP) approach taking the forward-backward algorithmic structure (FB), has demonstrated state-of-the-art performance in monochromatic RI imaging by alternating a data-fidelity step with a regularisation step via learned denoisers. In this work, we introduce HyperAIRI, its hyperspectral extension, underpinned by learned hyperspectral denoisers enforcing a power-law spectral model. For each spectral channel, the HyperAIRI denoiser takes as input its current image estimate, alongside estimates of its two immediate neighbouring channels and the spectral index map, and provides as output its associated denoised image. To ensure convergence of HyperAIRI, the denoisers are trained with a Jacobian regularisation enforcing non-expansiveness. To accommodate varying dynamic ranges, we assemble a shelf of pre-trained denoisers, each tailored to a specific dynamic range. At each HyperAIRI iteration, the spectral channels of the target image cube are updated in parallel using dynamic-range-matched denoisers from the pre-trained shelf. The denoisers are also endowed with a spatial image faceting functionality, enabling scalability to varied image sizes. Additionally, we formally introduce Hyper-uSARA, a variant of the optimisation-based algorithm HyperSARA, promoting joint sparsity across spectral channels via the $\ell_{2,1}$ -norm, also adopting FB. We evaluate HyperAIRI’s performance on simulated and real observations. We showcase its superior performance compared to its optimisation-based counterpart Hyper-uSARA, CLEAN’s hyperspectral variant in WSClean, and the monochromatic imaging algorithms AIRI and uSARA. HyperAIRI’s MATLAB implementation is available in the [BASPLib](#) code library.

Key words: techniques: image processing – techniques: interferometric.

1 INTRODUCTION

Radio interferometry is a powerful technique in astronomy, providing high-resolution views of the sky by combining signals from an array of antennas. In particular, the upcoming Square Kilometre Array ([SKA](#), [Scaife 2020](#)) is designed to deliver unprecedented sensitivity and resolution, with phase 1 offering more than a tenfold improvement compared to its precursor instruments, [MeerKAT](#) ([Jonas 2009](#)) and Australian SKA Pathfinder ([ASKAP](#), [Hotan et al. 2021](#)). These telescopes observe across wide frequency bands by collecting Fourier measurements, enabling the study of astrophysical processes at both spatial and spectral scales.

However, the associated inverse problem of hyperspectral image reconstruction is inherently ill-posed due to incomplete Fourier sampling, instrumental noise, and calibration errors. Monochromatic algorithms, which reconstruct spectral channels independently, achieve only limited recovery under such conditions. In contrast, joint-channel reconstruction exploits spectral correlations to regularise the ill-posed problem and enables high-precision recovery, particularly in high-dynamic-range (HDR) scenarios. Nevertheless, the sheer scale of hyperspectral data and the need for precise imaging

significantly increase the computational demands, calling for efficient and scalable algorithms with joint-channel reconstruction capability.

Most radio sources emit synchrotron radiation that can be described by a power-law spectral model ([Thompson et al. 2017](#)). Building on the celebrated CLEAN algorithm ([Högbom 1974](#)), its first hyperspectral extension, Multi-Frequency (MF) CLEAN, models spectral variations via polynomial functions, and solves for the corresponding coefficient images during reconstruction ([Sault & Wieringa 1994](#)). Further improvements are enabled by combining MF with Multi-Scale (MS) CLEAN ([Cornwell 2008](#)), enhancing the recovery of extended emission ([Rau & Cornwell 2011](#); [Offringa & Smirnov 2017](#)). However, low-order polynomials are often inadequate to capture complex spectral behaviour ([Scaife & Heald 2012](#)). To address this, [Ceccotti et al. \(2023\)](#) have injected a forced-spectrum fitting approach within CLEAN, enforcing a prior spectral knowledge directly during reconstruction. While computationally efficient, CLEAN-based algorithms still fall short in achieving precise imaging, *i.e.* high-resolution and high-sensitivity imaging. These limitations stem from their simplistic prior model: spatial resolution remains constrained by the instrument’s nominal resolution, and dynamic range is degraded by the addition of residuals in the final reconstruction.

Bayesian inference methods, such as the variational Bayes ap-

* E-mail: y.wiaux@hw.ac.uk.

proach underpinning the RESOLVE algorithm (Junklewitz et al. 2016), have demonstrated superior precision and robustness over CLEAN-based techniques (Arras et al. 2021; Roth et al. 2023). Assuming a first-order power-law spectral model, Junklewitz et al. (2015) proposed the joint estimation of a reference-frequency image and a spectral index map. Although these methods naturally provide uncertainty quantification functionality, their scalability and precision on large-scale observations remain to be demonstrated.

Methods rooted in optimisation theory have shown promise in astronomical imaging, offering precision imaging. Optimisation provides a robust and versatile framework to address ill-posed inverse problems, typically formulated as minimisation tasks solved via convergent iterative algorithmic structures. In this context, the reconstructed image is obtained as the minimiser of an objective function composed of a data fidelity function and a regularisation function encoding sophisticated image models. Optimisation offers a multitude of distributed algorithmic structures for parallelised reconstruction at scale. Among these methods, the SARA family of algorithms leverages sparsity-based priors, demonstrating superior imaging quality compared to CLEAN across diverse imaging scenarios (Carrillo et al. 2012; Onose et al. 2016, 2017; Repetti et al. 2017; Birdi et al. 2018; Pratley et al. 2018; Dabbech et al. 2018; Terris et al. 2023; Wilber et al. 2023a). Specifically, HyperSARA, promotes joint-channel average sparsity of the hyperspectral image cube in a redundant wavelet dictionary, and its low-rankness (Abdulaziz et al. 2016, 2019). HyperSARA takes the primal-dual forward-backward algorithmic structure (PD-FB, Condat 2013), which enables full splitting of the functions involved, and parallel updates of the dual variables. To further improve scalability to large image sizes, Thouvenin et al. (2023a) proposed its faceted variant operating on 3D spatio-spectral image facets. The algorithm has been validated on real observational data, demonstrating state-of-the-art reconstruction (Thouvenin et al. 2023b). Yet, HyperSARA requires heavy cross-channel communications and could introduce significant overhead for extreme-scale problems. In this work, we introduce another simpler variant of HyperSARA, dubbed Hyper-uSARA, which adopts an unconstrained formulation of the minimisation task, thereby eliminating the need for exact noise distribution knowledge. It also takes a simpler algorithmic structure, the FB (Combettes & Pesquet 2011), alternating data fidelity and regularisation steps, while still allowing for full parallelisation within each step.

Recently, deep learning has gained increasing attention in RI imaging for its ability to produce reconstructions with rapid inference. Existing approaches focus on monochromatic imaging. These include traditional, end-to-end neural networks, either reconstructing images from back-projected data (Connor et al. 2022; Gheller & Vazza 2022) or post-processing sub-optimal outputs from other algorithms such as CLEAN (Terris et al. 2019). However, these methods often lack precision, robustness, and interpretability (Goodfellow et al. 2014; Nguyen et al. 2015; Pang et al. 2018). Conditioned denoising diffusion probabilistic models have also been explored for RI imaging (Wang et al. 2023; Drozdova et al. 2024). They face similar issues and remain in early development.

Advanced architectures such as unrolling Deep Neural Networks (DNN) promote data consistency and possibly algorithmic stability by unfolding a fixed number of iterations of an optimisation algorithm as key modules within the network (Monga et al. 2021). These networks are trained end-to-end while preserving an explicit link to optimisation theory. However, existing unrolling schemes remain limited by their fixed iteration count, and lack formal convergence guarantees. Furthermore, embedding computationally-intensive measure-

ment operators directly into the network can make training prohibitively expensive.

In contrast, the Plug-and-Play (PnP) framework bridges optimisation theory and deep learning (Venkatakrishnan et al. 2013; Romano et al. 2017; Reehorst & Schniter 2018) offering a more flexible and robust alternative. In this approach, proximal operators enforcing handcrafted regularisations within an optimisation algorithm are replaced by learned DNN denoisers. These denoisers can be agnostic to the measurement process, making them adaptable to diverse configurations in RI imaging. Among these, the AIRI family of PnP algorithms (Terris et al. 2023, 2025) for monochromatic RI imaging, endowed with convergence guarantees (Pesquet et al. 2021). AIRI has been validated on both simulated and real wide-field observational data (Dabbech et al. 2022; Wilber et al. 2023b). Thanks to their convolutional architecture and compact receptive fields, AIRI denoisers are typically trained on small image patches, and seamlessly applied to images of arbitrary size during inference. Additionally, they can be easily applied in parallel to image facets for scalability. These properties make AIRI well suited to large-scale, precision imaging.

Inspired by unrolled networks and PnP algorithms, Aghabiglou et al. (2024) have recently proposed R2D2, a novel imaging paradigm for radio interferometry. R2D2 is underpinned by a series of iteration-specific DNNs, each taking as input the current image estimate and associated data residual. The final reconstruction is formed by summing the DNNs' output. In contrast to unrolled networks, R2D2 decouples data fidelity from the network architecture thereby avoiding the associated computational challenges. Conceptually, it can be interpreted as a learned version of CLEAN (Dabbech et al. 2024), substituting CLEAN's minor cycles with iteration-specific DNNs. The novel paradigm has demonstrated superior imaging precision to the state of the art in field, namely AIRI and uSARA, both in simulation and on real data, only at a fraction of their computational cost. However, early incarnations of R2D2 have been so far trained in a telescope-specific setting, and for monochromatic intensity imaging at small scale. Extending it to large scale wideband imaging poses additional challenges that remain to be addressed.

Building on the precision and scalability of AIRI, we propose HyperAIRI, a novel PnP algorithm tailored for high-precision hyperspectral RI imaging. HyperAIRI applies learned denoisers to each spectral channel in parallel with side information from neighbouring channels. The reconstruction approach further enhances spectral coherence by incorporating a physical power-law model, with the spectral index map either estimated on the fly during reconstruction or provided as an input. This design ensures local communication at each iteration and requires global communication only during spectral index updates, making HyperAIRI highly scalable and efficient in distributed high-performance computing (HPC) environments. Similarly to AIRI, HyperAIRI takes FB, with convergence guaranteed by the non-expansiveness of the denoisers, enforced via a Jacobian regularisation term in the training loss. We provide a shelf of pre-trained denoisers covering a wide dynamic-range, eliminating the need for problem-specific training. We demonstrate the superior performance of HyperAIRI, compared with state-of-the-art methods in the field, including the optimisation-based Hyper-uSARA and joint-channel CLEAN, on simulated the Very Large Array (VLA, Perley et al. 2011) data and real ASKAP observations.

The remainder of this paper is organised as follows. In Section 2, we formalise the hyperspectral RI imaging problem. Section 3 reviews the hyperspectral SARA prior and formulates the Hyper-uSARA algorithm. Section 4 presents the HyperAIRI algorithm, including the network architecture, training methodology, and overall algorithm structure. Section 5 reports experimental results on simu-

lated datasets to assess HyperAIRI's performance under controlled conditions. Section 6 demonstrates its application to real ASKAP observations. Finally, Section 7 summarises the contributions and discusses potential directions for future work.

2 HYPERSPECTRAL RI IMAGING

In this section, we present the power-law spectral model of the radio emission, examine the specificity of the hyperspectral Fourier sampling, and formulate the corresponding measurement model that defines the RI inverse problem.

2.1 Hyperspectral radio emission model

In radio astronomy, continuum synchrotron emission typically varies smoothly with frequency, with flux density scaling according to a power-law (Thompson et al. 2017). This makes the power-law spectral model a practical choice for parametrizing the hyperspectral RI image cube. To account for sudden changes in the spectrum while still preserving overall spectral smoothness across a wide frequency range, a second-order term is introduced in the exponent (Rau & Cornwell 2011). Consider a reference spectral frequency ν_0 and the corresponding channel image $\bar{x}_0 \in \mathbb{R}^N$. At a given frequency ν_l , the radio image $\bar{x}_l \in \mathbb{R}^N$ can be modelled as

$$\bar{x}_l = \bar{x}_0 \left(\frac{\nu_l}{\nu_0} \right)^{-\alpha + \beta \log\left(\frac{\nu_l}{\nu_0}\right)} \quad (1)$$

where $\alpha \in \mathbb{R}^N$ is the spectral index map and $\beta \in \mathbb{R}^N$ is the spectral curvature map.

This model is widely used for characterizing various radio sources, including galaxies, which yield different spectral indexes due to the different physical radiation mechanisms (De Gasperin et al. 2018). Furthermore, it can serve as a physics-informed prior in the reconstruction of the hyperspectral image cube, ensuring meaningful correlations across different spectral channels (Junklewitz et al. 2015; Ceccotti et al. 2023).

2.2 Hyperspectral Fourier sampling in RI

When probing the radio sky, RI measurements are acquired using arrays of antennas operating at multiple spectral channels. At a given observation frequency, each pair of antennas captures a noisy spatial Fourier intensity measurement, also known as a visibility. The corresponding Fourier mode is derived from the projection of the associated baseline onto the plane orthogonal to the line of sight, denoted by \bar{b} in the unit of meters (Thompson et al. 2017). The collection of visibilities from all baselines, accumulated over time, forms the so-called uv -coverage. For a given channel $l \in \{1, \dots, L\}$, the probed Fourier mode b_l is described in the unit of the observation wavelength such that

$$b_l = \frac{\nu_l}{c} \bar{b}, \quad (2)$$

where ν_l is the observation frequency, and c is the speed of light. Consequently, for a fixed set of baselines, the uv -coverage becomes more concentrated towards the centre of the Fourier plane, *i.e.* focusing on the low spatial Frequency content, at the lower end of the observation frequency bandwidth. At the higher end of the observation frequency bandwidth, the same sampling pattern dilates radially away from the centre of the Fourier plane, *i.e.* acquiring the high spatial Frequency

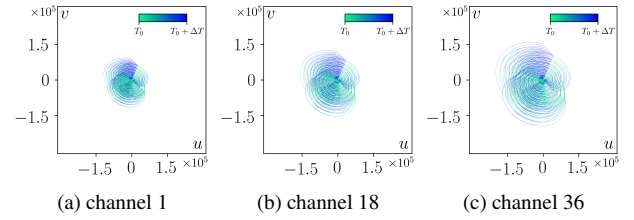


Figure 1. A set of simulated VLA hyperspectral sampling patterns of different channels. The three panels show the normalised uv sampling patterns for the first, middle and last channels of an observation with frequencies 1.00, 1.34 and 1.70 GHz, respectively. The coordinates are in the unit of wavelength.

content. Figure 1 shows this spectral-frequency-dependent expansion of the uv -sampling pattern across three representative channels in a simulated VLA uv -coverage. By design, observations at lower-frequency channels are characterised by lower spatial resolution but higher sensitivity, and conversely, higher-frequency channels offer higher resolution but lower sensitivity due to the scaling of the uv -coverage.

2.3 RI hyperspectral inverse problem

Focusing on intensity imaging and assuming a narrow field of view without atmospheric or instrumental perturbations, at a given spectral channel l , the process of measuring visibilities $y_l \in \mathbb{C}^M$ from the true sky intensity image $\bar{x}_l \in \mathbb{R}_+^N$ can be modelled by the following discrete linear system:

$$y_l = \Phi_l \bar{x}_l + n_l, \text{ with } \Phi_l = \mathbf{G}_l \mathbf{F} \mathbf{P}, \quad (3)$$

where $\Phi_l \in \mathbb{C}^{M \times N}$ represents the measurement operator at channel l , and $n_l \in \mathbb{C}^M$ denotes measurement noise, modelled as a complex white Gaussian noise with mean zero and a standard deviation of τ_l . The measurement operator Φ_l models incomplete non-uniform Fourier sampling where $\mathbf{G}_l \in \mathbb{C}^{M \times N'}$ is a sparse non-uniform Fourier interpolation matrix, with each row corresponding to a compact convolutional interpolation kernel centred at the corresponding Fourier mode, $\mathbf{F} \in \mathbb{R}^{N' \times N'}$ denotes the 2D Fourier transform, and $\mathbf{P} \in \mathbb{R}^{N' \times N}$ is a zero-padding operator, also encompassing the correction for the convolutional interpolation kernels (Fessler & Sutton 2003).

In practice, the noise n_l may be non-white, in which case a diagonal noise-whitening matrix $\Theta_l \in \mathbb{R}_+^M$ is incorporated into Φ_l and applied to the measurements y_l , such that $\Phi_l = \Theta_l \mathbf{G}_l \mathbf{F} \mathbf{P}$. Each diagonal element of Θ_l is the inverse of the noise standard deviation of the corresponding visibility. With this adjustment known as natural weighting, the linear measurement model in (3) remains valid for the whitened visibilities y_l , whereby $\tau_l = 1$. On a further note, the RI measurement process can be affected by the so-called w -effect, a phase modulation arising from the non-coplanarity of the antenna array which is non-negligible in wide-field imaging. In this context, the operator Φ_l can account for this effect via additional row-wise convolutions (Dabbech et al. 2017).

In what follows, the hyperspectral visibilities, image cube, and measurement noise are arranged in a matrix form as $\mathbf{Y} = (y_1, \dots, y_L) \in \mathbb{R}^{M \times L}$, $\mathbf{X} = (x_1, \dots, x_L) \in \mathbb{R}^{N \times L}$, and $\mathbf{N} = (n_1, \dots, n_L) \in \mathbb{R}^{M \times L}$ respectively. The hyperspectral measurement operator is defined such that $\Phi(\mathbf{X}) = ([\Phi_l x_l]_{1 \leq l \leq L})$. Using this notation, the hyperspectral RI measurement model becomes:

$$\mathbf{Y} = \Phi(\mathbf{X}) + \mathbf{N}. \quad (4)$$

Hyperspectral RI imaging aims to jointly reconstruct the spatial and

spectral information of the radio emission encapsulated in the hyperspectral cube \mathbf{X} from the incomplete and noisy measurements \mathbf{Y} . It is evident from (3) that the hyperspectral RI measurement process is separable across channels, allowing monochromatic algorithms to reconstruct each spectral channel independently. However, joint spectral imaging methods can yield higher-quality reconstructions by leveraging the higher sensitivity of lower-frequency channels and the improved resolution of higher-frequency channels.

3 OPTIMISATION-BASED HYPERSPECTRAL IMAGING

Building on HyperSARA, we introduce its unconstrained variant, Hyper-uSARA, tailored for hyperspectral imaging with unknown noise statistics and calibration errors. This variant is particularly well suited to large-scale real observational data, where flexibility and efficiency are critical. We begin by revisiting the optimisation theory underpinning our method, focusing on the FB for solving unconstrained minimisation problems. We then describe the hyperspectral SARA prior, which promotes joint-channel average sparsity, and present the full algorithmic structure of Hyper-uSARA.

3.1 Optimisation theory

The linear measurement model taking the form (4) is widely used across various imaging tasks, such as denoising, super-resolution, inpainting, image deblurring, and magnetic resonance imaging. While the measurement operator $\Phi(\cdot)$ varies across image modalities, the underlying inverse problem is often ill-posed due to incomplete and noisy measurements. Optimisation methods are thus appealing for their versatility in regularising inverse problems by injecting sophisticated image models.

Within the convex optimisation framework, the inverse problem is addressed by solving a minimisation problem with objective function

$$\min_{\mathbf{X} \in \mathbb{R}^{N \times L}} f(\mathbf{X}) + \lambda r(\mathbf{X}) \quad (5)$$

where $f : \mathbb{R}^{N \times L} \mapsto \mathbb{R} \in \Gamma_0(\mathbb{R}^{N \times L})^1$ is the data-fidelity term reflecting the linear measurement model, $r : \mathbb{R}^{N \times L} \mapsto \mathbb{R} \in \Gamma_0(\mathbb{R}^{N \times L})$ is the regularisation term enforcing the image model. Given the Gaussian nature of the measurement noise, a squared-error fidelity term is one common choice for f , such that $f(\mathbf{X}) = \frac{1}{2} \|\Phi(\mathbf{X}) - \mathbf{Y}\|_F^2$, where $\|\cdot\|_F$ denotes Frobenius norm. The parameter $\lambda > 0$ is a regularisation parameter balancing the two terms. Inserting f into (5) yields an unconstrained minimisation task.

When at least one of the two terms is differentiable—in this case the data fidelity term f —problems of the form (5) can be solved with FB. The iteration structure consists of a gradient descent step (forward) for the differentiable data-fidelity term, followed by a denoising step (backward) via the proximity operator of the non-differentiable regularisation term. At any iteration i , the image cube update reads:

$$\mathbf{X}^{i+1} = \text{prox}_{\gamma, \lambda r}(\mathbf{X}^i - \gamma \nabla f(\mathbf{X}^i)). \quad (6)$$

The gradient of $f(\cdot)$ reads $\nabla f(\mathbf{X}) = \text{Re}\{\Phi^\dagger(\Phi(\mathbf{X}))\} - \text{Re}\{\Phi^\dagger(\mathbf{Y})\}$, where $\Phi^\dagger(\cdot)$ is the adjoint of hyperspectral measurement operator and $\mathbf{X}^{\text{dirty}} = \text{Re}\{\Phi^\dagger(\mathbf{Y})\}$ is the back-projected data, commonly referred

¹ $\Gamma_0(\mathbb{R}^{N \times L})$ denotes the set of convex, proper, and lower semi-continuous functions from $\mathbb{R}^{N \times L}$ to $(-\infty, \infty)$.

to as the dirty image cube. The parameter γ is the step size, upper-bounded by $2/\|\Phi^\dagger(\Phi(\cdot))\|_S^2$ to ensure the algorithm's convergence, with $\|\cdot\|_S$ denoting the spectral norm (Bauschke et al. 2017).

By definition, the proximity operator of a regularisation function r is given by

$$\text{prox}_r(\mathbf{Z}) = \underset{\mathbf{U} \in \mathbb{R}^{N \times L}}{\operatorname{argmin}} \frac{1}{2} \|\mathbf{U} - \mathbf{Z}\|_F^2 + r(\mathbf{U}). \quad (7)$$

When r is separable across channels, *i.e.* taking the form $r(\mathbf{X}) = \sum_{l=1}^L r_l(x_l)$, naturally the problem (5) decomposes into L independent monochromatic imaging problems. To exploit spectral correlations and improve reconstruction quality, joint regularisation terms are preferred for hyperspectral RI imaging.

3.2 Hyperspectral SARA prior and Hyper-uSARA

The choice of the prior encoded via the regularisation function r in (5) greatly affects imaging precision. In monochromatic RI imaging, the sparsity-based SARA prior promotes average sparsity of the sought image across a collection of 8 orthonormal wavelet bases and the Dirac basis, denoted as $\Psi \in \mathbb{R}^{N \times bN}$ with $b = 9$. Its extension to hyperspectral imaging, the HyperSARA prior, is underpinned by the assumption that the image cube is the combination of a few radio sources, each having a distinct spectral behaviour (Abdulaziz et al. 2019). As such, the HyperSARA prior promotes the low-rankness of the image cube, whose rank is upper-bounded by the number of radio sources, and its joint-sparsity over the spectral channels in the SARA dictionary. The former is enforced via a nuclear norm which penalises the ℓ_1 -norm of the vector of the singular values of \mathbf{X} . The latter is enforced via a $\ell_{2,1}$ -norm, defined as the ℓ_1 -norm of the vector whose elements are the ℓ_2 -norms of the rows of $\Psi^\dagger \mathbf{X}$. Focusing on intensity imaging, the prior also includes non-negativity of the target image cube. The HyperSARA algorithm takes a constraint minimisation task, involving bounds on the hyperspectral noise cube, and is solved using the PD-FB.

Underpinned by a constrained data fidelity term, HyperSARA requires accurate knowledge of the noise statistics, which can be challenging in practice, with calibration errors often dominating the theoretical noise. To address this, we formally propose the unconstrained formulation of the HyperSARA minimisation task. Furthermore, we discard the low-rankness term, though accepting a slight loss in precision, since it involves singular value decomposition of the image cube estimate at every iteration, a computationally expensive operation for large-scale imaging even when adopting 3D faceting as in Faceted HyperSARA (Thouvenin et al. 2023a,b). This simplification also eliminates the need to balance the average joint-sparsity and low-rankness terms, while reducing the number of regularisation parameters. The resulting unconstrained variant of HyperSARA underpinned by an average joint-sparsity prior is dubbed Hyper-uSARA. The regularisation function reads

$$r(\mathbf{X}) = \sum_{n=1}^{bN} \epsilon \log \left(\epsilon^{-1} \|((\Psi^\dagger \mathbf{X})^\top)_n\|_2 + 1 \right) + \iota_{\mathbb{R}_+^{N \times L}}(\mathbf{X}), \quad (8)$$

where ϵ is a hyper parameter, $(\cdot)_n$ represent the n -th column of the argument matrix, $\|\cdot\|_2$ denotes the ℓ_2 -norm, and $\iota_{\mathbb{R}_+^{N \times L}}(\cdot)$ is an indicator function³ imposing positivity constraint on each pixel. To

² In practice, γ is typically fixed to $1.98/\|\Phi^\dagger(\Phi(\cdot))\|_S$.

³ The indicator function $\iota_{\mathbb{R}_+^{N \times L}}(\mathbf{X}) = 0$ if all elements in \mathbf{X} are positive, otherwise $\iota_{\mathbb{R}_+^{N \times L}}(\mathbf{X}) = \infty$.

address the non-convex regularisation function r , the minimisation problem of the form (5) is addressed via a re-weighting scheme that iteratively solves a sequence of convex minimisation tasks. More precisely, at each re-weighting iteration a minimisation task involving a surrogate convex regularisation function \tilde{r} instead of r (Repetti & Wiaux 2021), such that

$$\tilde{r}(\mathbf{X}) = \|\Psi^\dagger \mathbf{X}\|_{2,1,\mathbf{w}} + \iota_{\mathbb{R}_+^{N \times L}}(\mathbf{X}). \quad (9)$$

The weighted average joint-sparsity regulariser is given by

$$\|\Psi^\dagger \mathbf{X}\|_{2,1,\mathbf{w}} = \left\| \mathbf{W} \sqrt{\sum_{l=1}^L (\Psi^\dagger \mathbf{x}_l)^2} \right\|_1, \quad (10)$$

where $\mathbf{W} \in \mathbb{R}^{bN \times bN}$ is a diagonal matrix, whose diagonal elements w_n form the vector $\mathbf{w} \in \mathbb{R}^{bN}$. The weights \mathbf{w} are updated at each re-weighting cycle from the solution of the preceding minimisation task as

$$\mathbf{w} = \epsilon \left/ \left(\epsilon + \sqrt{\sum_{l=1}^L (\Psi^\dagger \mathbf{x}_l)^2} \right) \right. \quad (11)$$

At each re-weighting iteration j , the objective function is updated using the current \mathbf{w}_j , and is solved via the FB (6). The Hyper-uSARA algorithm is summarised in Algorithm 1. The proximity operator of the composite regularisation function (9) is computed via a sub-iterative dual-FB (Combettes & Pesquet 2011) illustrated in Algorithm 2. At a given $\mathbf{Z} \in \mathbb{R}^{N \times L}$, the respective proximity operators for the positivity constraint and the weighted $\ell_{2,1}$ -norm sparsity term have closed-form solutions such that

$$\text{prox}_{\iota_{\mathbb{R}_+^{N \times L}}(\cdot)}(\mathbf{Z}) = \max\{\mathbf{Z}, \mathbf{0}\}, \quad (12)$$

and

$$\text{prox}_{\eta \|\cdot\|_{1,2,\mathbf{w}}}(\mathbf{Z}) = \left(\left[\max \left\{ \|\mathbf{(Z}^\top)_n\|_2 - \eta w_n, 0 \right\} \frac{(\mathbf{Z}^\top)_n}{\|(\mathbf{Z}^\top)_n\|_2} \right]_{1 \leq n \leq N} \right)^\top. \quad (13)$$

As in Faceted-HyperSARA, the average joint-sparsity regularisation is applied in parallel to each 3D image facet using the same splitting strategy. Formally, the FB gradient step only requires the dirty image and the application of $\Phi^\dagger(\Phi(\cdot))$, keeping memory and computational cost tied to the image size (Vijay Kartik et al. 2017). Hence, Hyper-uSARA can achieve better efficiency for large-scale imaging tasks under tight computational constraints.

Concerning the choice of the regularisation parameters involved, both λ and ϵ are inferred from the image domain noise level. Terris et al. (2023) proposed estimating the image domain noise level at each frequency channel as

$$\sigma_{\text{heu},l} = \tau_l \left/ \sqrt{2\|\Phi_l\|_S^2} \right. \quad (14)$$

Under this consideration, and following Thouvenin et al. (2023a), the noise floor level ϵ in the ℓ_2 -norm of the wavelet coefficients is then approximated such that

$$\epsilon^2 = \sum_{l=1}^L \sigma_{\text{heu},l}^2 / b, \quad (15)$$

and the regularisation parameter is chosen as $\lambda = \epsilon/\gamma$ (Thouvenin et al. 2023a).

Algorithm 1 Hyper-uSARA

```

1: given  $\mathbf{X}^0, \mathbf{X}^{\text{dirty}}, \Phi(\cdot), \Phi^\dagger(\cdot)$  // Initialisation
2: given  $\gamma, \lambda, \epsilon$  // Step size, regularisation parameter, noise floor level
3: given  $\xi_1, \xi_2$  // Tolerance for re-weighting and FB
4: given  $J, I$  // Maximum iterations for re-weighting and FB
5: // Re-weighting loop
6: repeat for  $j = 1, 2, \dots, J$ 
7:    $\mathbf{w}^j = \epsilon \left/ \left( \epsilon + \sqrt{\sum_{l=1}^L (\Psi^\dagger \mathbf{x}_l^{j-1})^2} \right) \right.$ 
8:   // FB loop
9:    $\mathbf{X}^{j,0} = \mathbf{X}^{j-1}$ 
10:  repeat for  $i = 1, 2, \dots, I$ 
11:     $\hat{\mathbf{X}}^{j,i} = \mathbf{X}^{j,i-1} - \gamma \text{Re} \left\{ \Phi^\dagger(\Phi(\mathbf{X}^{j,i-1})) - \mathbf{X}^{\text{dirty}} \right\}$ 
12:     $\mathbf{X}^{j,i} = \text{prox}_{\gamma, \lambda, \tilde{r}}(\hat{\mathbf{X}}^{j,i})$  // Using Algorithm 2
13:    until  $\|\mathbf{X}^{j,i} - \mathbf{X}^{j,i-1}\|_F / \|\mathbf{X}^{j,i-1}\|_F < \xi_2$ 
14:   $\mathbf{X}^j = \mathbf{X}^{j,i}$ 
15: until  $\|\mathbf{X}^j - \mathbf{X}^{j-1}\|_F / \|\mathbf{X}^{j-1}\|_F < \xi_1$ 
16: return  $\mathbf{X}^J$ 

```

Algorithm 2 Solving proximity operator of (9) with dual-FB

```

1: given  $\mathbf{X}^0, \hat{\mathbf{X}}, \Psi, \Psi^\dagger, \mathbf{w}$  // Initialisation
2: given  $\gamma, \lambda$  // Step size and regularisation parameter
3: given  $\xi_3$  // Tolerance for dual-FB
4: given  $K$  // Maximum iterations for dual-FB
5:  $\mathbf{V}^0 = \Psi^\dagger(\mathbf{X}^0)$ 
6: repeat for  $k = 1, 2, \dots, K$ 
7:    $\mathbf{X}^k = \text{prox}_{\iota_{\mathbb{R}_+^{N \times L}}(\cdot)}(\hat{\mathbf{X}} - \Psi(\mathbf{V}^{k-1}))$ 
8:    $\hat{\mathbf{V}}^k = \mathbf{V}^{k-1} + \Psi^\dagger(\mathbf{X}^k)$ 
9:    $\mathbf{V}^k = \hat{\mathbf{V}}^k - \text{prox}_{\gamma, \lambda, \|\cdot\|_{1,2,\mathbf{w}}}(\hat{\mathbf{V}}^k)$ 
10:  until  $\|\mathbf{X}^k - \mathbf{X}^{k-1}\|_F / \|\mathbf{X}^{k-1}\|_F < \xi_3$ 
11: return  $\mathbf{X}^k$ 

```

4 HYPERAIRI

In this section, we present the HyperAIRI algorithm, which can be seen as the PnP counterpart of Hyper-uSARA within the PnP-FB. We subsequently detail the architecture of HyperAIRI denoisers and the associated training strategy, and we formalise the algorithmic structure of our proposed approach.

4.1 Hyperspectral PnP-FB and HyperAIRI denoiser

By definition, the proximal operator associated with a regularisation function (7) can be interpreted as solving a denoising problem. PnP algorithms build on this insight by replacing the proximal operator with a pretrained DNN, typically trained for image denoising (Venkatakrishnan et al. 2013). In the case of additive Gaussian noise, the denoising problem consists of estimating the ground truth $\bar{\mathbf{U}}$ from the noisy measurement \mathbf{Z} , modelled as

$$\mathbf{Z} = \bar{\mathbf{U}} + \sigma \mathbf{E} \quad (16)$$

where $\mathbf{E} \sim \mathcal{N}(0, \mathbf{I})$ is a realisation of a white Gaussian noise cube with standard deviation and σ . By construction, the trained denoisers are blind to the measurement process, and can therefore adapt easily to RI imaging for different telescopes and under varying observational conditions. AIRI (Terris et al. 2023, 2025) is a successful instantiation of PnP algorithms for monochromatic RI imaging. By replacing the handcrafted proximity operators in FB with learned firmly

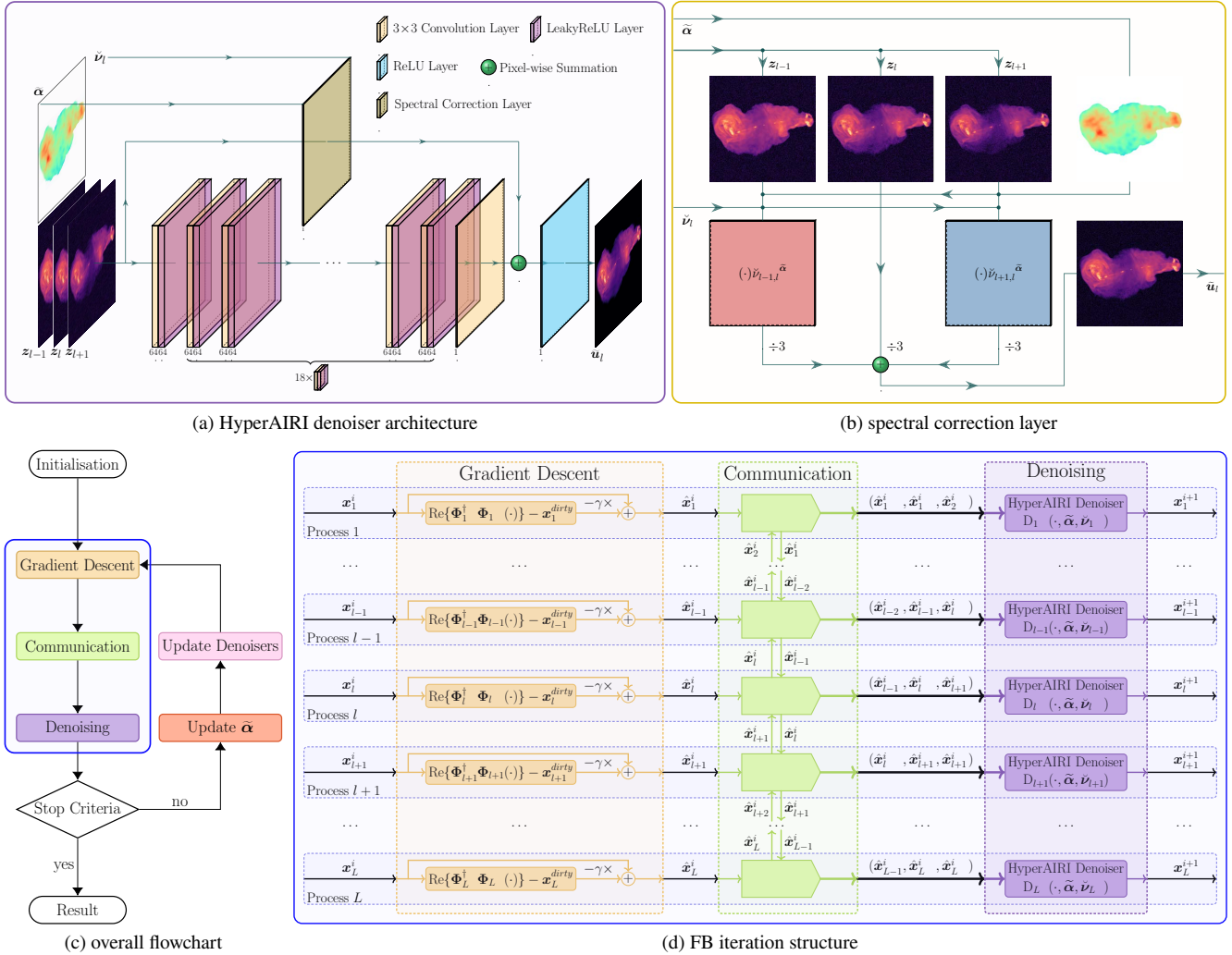


Figure 2. HyperAIRI algorithm structure. Panels illustrate the following: (a) HyperAIRI denoiser architecture; (b) the inner structure of the spectral correction layer; (c) the flowchart of HyperAIRI algorithm; and (d) HyperAIRI’s FB iteration structure.

non-expansive denoisers⁴, AIRI provides state-of-the-art imaging precision, preserving the robustness of optimisation algorithms and the flexibility of PnP algorithms. Building on the monochromatic AIRI design, HyperAIRI adopts the PnP-variant of (6), which reads

$$\mathbf{X}^{i+1} = \mathbf{D}(\mathbf{X}^i - \gamma \nabla f(\mathbf{X}^i)), \quad (17)$$

where $\mathbf{D}(\cdot)$ represents denoising via a trained DNN denoiser.

Furthermore, we adapt AIRI’s network architecture to accommodate multi-channel input and exploit spectral correlations. In hyperspectral RI imaging, the number of spectral channels can vary widely. Applying the DNN along the spectral axis via an overlapping window provides a flexible approach, decoupling the number of DNN input channels from the size of the target image cube during image reconstruction. This design also supports channel-wise parallelisation when denoising, albeit each denoiser only leverages correlations within its immediate neighbours. To mitigate the potential

sub-optimality of this local joint denoising, the power-law spectral model is introduced to propagate global spectral information.

The architecture of a HyperAIRI denoiser takes a variation of the DnCNN for AIRI containing 20 convolutional layers. To denoise a channel l of a noisy image cube \mathbf{Z} , HyperAIRI denoiser takes as input (i) the sub-cube composed of the target channel z_l and its two adjacent channels, (ii) the frequency ratios between the neighbouring and target channels, and (iii) the estimated spectral index map. It then outputs the denoised image \tilde{z}_l . HyperAIRI denoiser injects the power-law spectral model underpinning the hyperspectral image cube via a spectral correction layer shown in Fig. 2(b). This layer takes the same set of inputs of HyperAIRI denoisers, providing as output the estimate of the target channel:

$$\tilde{u}_l = \frac{1}{3} \left(z_{l-1} \check{\nu}_{l-1,l} \tilde{\alpha} + z_l + z_{l+1} \check{\nu}_{l+1,l} \tilde{\alpha} \right), \quad (18)$$

where $\check{\nu}_{l-1,l} = \nu_{l-1}/\nu_l$ and $\check{\nu}_{l+1,l} = \nu_{l+1}/\nu_l$. In the spectral correction layer, only the spectral index map is involved, while the spectral curvature map is delegated implicitly to the other layers. This separation supports the numerical stability of the entire algorithm, especially in cases where $\tilde{\alpha}$ is estimated dynamically during reconstruction. The remaining layers in the DNN are designed to predict the residual difference between the initial estimate and the ground-truth image.

⁴ An operator $\mathbf{D}(\cdot)$ is firmly non-expansive if it satisfies the condition: $\|\mathbf{D}(\mathbf{a}) - \mathbf{D}(\mathbf{b})\|^2 \leq \langle \mathbf{D}(\mathbf{a}) - \mathbf{D}(\mathbf{b}), \mathbf{a} - \mathbf{b} \rangle$. Intuitively, this means $\mathbf{D}(\cdot)$ moves inputs closer together while generally preserving their relative directions.

The final estimate of the HyperAIRI denoiser is the summation of the predicted difference and the output of the spectral correlation layer with positivity constraint from ReLU layer. The full architecture is shown in Fig. 2(a).

As HyperAIRI denoiser targets single-channel output with similar numbers of learnable parameters, the training and inference costs are comparable to those of AIRI, maintaining its computational efficiency. Moreover, this sliding-window denoising strategy provides the flexibility to process image cubes of varying sizes. Thus, the proposed HyperAIRI denoiser structure meets our requirements for efficiency and flexibility.

4.2 Training HyperAIRI denoisers

To address the limited availability of training data for hyperspectral RI imaging, we build a training dataset based on the two monochromatic datasets proposed by Terris et al. (2025), namely the Optical Astronomical Image Dataset (OAID) and the Magnetic Resonance Image Dataset (MRID). Both datasets contain 5,000 images of size 512×512 pixels, and are used jointly during training. For each monochromatic image, a corresponding hyperspectral image cube is generated according to the power-law model in (1). Following Thouvenin et al. (2023a), the curvature map β is modelled as a random Gaussian field, while the spectral index map α is derived from the logarithm of a Gaussian-blurred version of $\bar{\mathbf{u}}$ combined with a random Gaussian field ensuring spatial correlation. The elements in α are in the range $[-5, 0]$ and those in β are in the range $[-0.5, 0.5]$. The simulated image cube $\bar{\mathbf{U}} \in \mathbb{R}^{N \times 3}$ is expressed as:

$$\bar{\mathbf{U}} = \left(\bar{\mathbf{u}} \check{\mathbf{v}}_{1,2}^{-\alpha+\beta \log \check{\mathbf{v}}_{1,2}}, \bar{\mathbf{u}}, \bar{\mathbf{u}} \check{\mathbf{v}}_{3,2}^{-\alpha+\beta \log \check{\mathbf{v}}_{3,2}} \right), \quad (19)$$

where $\check{\mathbf{v}}_{1,2}$ and $\check{\mathbf{v}}_{3,2}$ are sampled uniformly from $[0.9, 1.0]$ and $[1.0, 1.1]$ respectively. The ratio 1.0 is included in the range to handle the boundary cases, where we duplicate the edge channels when denoising an image cube, resulting in frequency ratios of 1.0.

HyperAIRI denoisers are trained in a supervised manner using pairs of the simulated groundtruth image cubes $\bar{\mathbf{U}}$ and their noisy versions \mathbf{Z} obtained following (16). As indicated by Terris et al. (2023, 2025), ensuring the non-expansiveness of the denoisers is crucial for the convergence of the final PnP algorithm in reconstructing HDR RI images. Therefore, the loss function includes a standard ℓ_1 loss and a Lipschitz regularisation term. Denoting the denoiser as \mathbf{D} with learnable parameters as θ , the training loss is

$$\begin{aligned} \mathcal{L}(\theta, \mathbf{Z}, \bar{\mathbf{U}}, \alpha, \check{\mathbf{v}}_2) = & \\ \| \mathbf{D}_\theta(\mathbf{Z}, \alpha, \check{\mathbf{v}}_2) - (\bar{\mathbf{U}})_2 \|_1 + \kappa \max\{ \| \nabla Q_\theta(\bar{\mathbf{U}}) \|_S, 1 - \delta \}, & \end{aligned} \quad (20)$$

where $(\cdot)_2$ selects the second channel of the image cube, α and $\check{\mathbf{v}}_2 = (\check{\mathbf{v}}_{1,2}, \check{\mathbf{v}}_{3,2})$ are the spectral index map and frequency ratios for \mathbf{U} . In the regularisation term, Q is defined as $2\mathbf{D}_\theta(\cdot, \alpha, \check{\mathbf{v}}_2) - (\cdot)_2$, and $\nabla Q(\cdot)$ denotes the Jacobian of Q . Here, $\kappa > 0$ is the regularisation parameter, and $\delta > 0$ determines the lower bound of the regularisation term.

To avoid retraining for each specific problem, a shelf of HyperAIRI denoisers can be trained across various σ values. In this work, we trained 6 DNNs at noise levels in the set $\{1.0 \times 10^{-5}, 2.0 \times 10^{-5}, 4.0 \times 10^{-5}, 8.0 \times 10^{-5}, 1.6 \times 10^{-4}, 3.2 \times 10^{-4}\}$ respectively, forming a shelf of HyperAIRI denoisers. Accompanied with proper scaling factors adaptively chosen during reconstructions, the denoisers will cover a dynamic range interval of $[1.6 \times 10^3, 1.0 \times 10^5]$.

Similarly to AIRI denoisers, HyperAIRI denoisers are trained using randomly cropped patches of size $46 \times 46 \times 3$ from the simulated image cubes to speed up the training process owing to their convolu-

tional nature. The compact receptive fields allows application to any image size during image reconstruction.

The training scripts are built with PyTorch in Python. Each HyperAIRI denoiser is trained for 5000 epochs with the ADAM optimiser (Kingma & Ba 2014). The initial learning rate is set to 10^{-4} , 10^{-5} and 10^{-6} for training noise levels 3.2×10^{-4} , $[4.0 \times 10^{-5}, 8.0 \times 10^{-5}, 1.6 \times 10^{-4}]$ and $[1.0 \times 10^{-5}, 2.0 \times 10^{-5}]$ respectively. The learning rate is halved every 900 epochs. The regularisation factor κ in (20) is also fine-tuned for each DNN to make sure the final value of the regularisation term is as close to 1 as possible. In practice, κ is typically close to the average value of the ℓ_1 loss term for optimal results. As suggested by Terris et al. (2023), we also use the weights of the DNNs trained with $\kappa = 0$ as initialisation to improve the training stability and the performance of the final DNNs.

4.3 Algorithmic structure

Plugging HyperAIRI denoisers trained at desired noise levels into the iterative FB forms the HyperAIRI algorithm. The detailed structure of our proposed algorithm is shown in Fig. 2(c).

4.3.1 Initialisation

In the initialisation stage, each channel selects an appropriate denoiser from the pre-trained denoiser shelf based on its dynamic range. As suggested by Terris et al. (2023, 2025), the inverse of the target dynamic range at channel l can be estimated as $\sigma_{\text{heu},l}/\tilde{\rho}_l$, where $\sigma_{\text{heu},l}$ is given in (14), and $\tilde{\rho}_l$ is the estimated maximum intensity of the image at channel l . As an initial estimation of $\tilde{\rho}_l$, we consider the maximum intensity of the dirty image normalised by the peak value of the point spread function (PSF), *i.e.*

$$\tilde{\rho}_l = \max \left(\mathbf{x}_l^{\text{dirty}} \right) / \max \left(\text{Re}\{\Phi_l^\dagger \Phi_l \delta\} \right) \quad (21)$$

where $\delta \in \mathbb{R}^N$ is a Dirac delta image with value 1 at its centre and 0 otherwise. For a given channel l , the denoiser with noise level σ closest to but smaller than $\sigma_{\text{heu},l}/\tilde{\rho}_l$ is chosen. To adjust for the difference between the inverse dynamic range of the image and the noise level of the selected denoiser, a scaling factor is applied (Dabbech et al. 2022):

$$D_l(\cdot, \tilde{\alpha}, \check{\mathbf{v}}_l) = \varrho_l D_\sigma(\cdot/\varrho_l, \tilde{\alpha}, \check{\mathbf{v}}_l), \quad (22)$$

with $\varrho_l = \sigma_{\text{heu},l}/\sigma$. Finally, the spectral index map $\tilde{\alpha}$ can be initialised to $\mathbf{0}$, derived from the dirty image, or specified by the user.

4.3.2 Reconstruction loop

At each iteration i , the process for channel l sends its gradient descent image $\hat{\mathbf{x}}_l^i$ to the adjacent channels ($l-1$ and $l+1$) and receives their corresponding images. These three images are combined to form the input cube $\hat{\mathbf{X}}_l^i = (\hat{\mathbf{x}}_{l-1}^i, \hat{\mathbf{x}}_l^i, \hat{\mathbf{x}}_{l+1}^i)$, which is then processed by the denoiser for channel l . Specific to edge channels, the processes for the first and last channels form image cubes by communicating with their only neighbour, resulting in $\hat{\mathbf{X}}_1^i = (\hat{\mathbf{x}}_1^i, \hat{\mathbf{x}}_2^i, \hat{\mathbf{x}}_1^i)$ and $\hat{\mathbf{X}}_L^i = (\hat{\mathbf{x}}_{L-1}^i, \hat{\mathbf{x}}_L^i, \hat{\mathbf{x}}_L^i)$ respectively. Thereafter, the denoisers for each channel are applied simultaneously to $\hat{\mathbf{X}}_l^i$. Random 90° rotations and flips, and the corresponding inverse transformations, are applied to the inputs and outputs of the DNNs, respectively, to exploit the transformation invariance of images (Terris et al. 2023). The result of the denoising step of all channels forms the image cube update \mathbf{X}_l^{i+1} .

4.3.3 Dynamic denoiser and spectral index map update

Following the standard FB update, the algorithm also updates the denoisers and the spectral index map dynamically. Initially, D_l is selected based on $\sigma_{\text{heu},l}$ using the maximum intensity of the normalised dirty image as $\tilde{\rho}_l$. However, this is a loose upper bound estimation of the real peak value ρ_l . To refine the estimate of $\sigma_{\text{heu},l}$, $\tilde{\rho}_l$ is updated as the maximum intensity of \mathbf{x}_l^{i+1} . $\sigma_{\text{heu},l}$ is monitored at each iteration to determine whether the current denoiser D_l and the corresponding scaling factor ϱ_l should be updated. [Terris et al. \(2025\)](#) has proven the effectiveness of this adaptive denoiser updating framework in monochromatic imaging. We adopt a similar strategy to update the estimate of the spectral index map $\tilde{\alpha}$ when needed, using the current estimate of the cube \mathbf{X}^i . Ignoring the spectral curvature term in (1), setting $v_0 = 1$ for simplicity and applying logarithm to both sides, the pixel n in channel l should follow

$$\log \mathbf{x}_l^i = -\tilde{\alpha} \log v_l + \log \mathbf{x}_0^i. \quad (23)$$

Then, a linear relationship between $\log \mathbf{x}_l$ and $\log v_l$ is anticipated. The slope of the linear function can be evaluated pixel-wise using linear regression, which yields $\tilde{\alpha}$, the estimated spectral index map. In practice, a smoothing 2D Gaussian kernel is applied to the image cube before gathering them for linear regression to ensure numerical stability. The 2D Gaussian kernel is fitted to the PSF's primary lobe at the highest-frequency channel, which represents the highest spatial resolution of the measurements. Furthermore, pixels with intensities below a preset threshold, taken as the minimal heuristic noise level of the entire image cube, are excluded from the estimation of $\tilde{\alpha}$.

4.3.4 Fully parallelised implementation

The entire HyperAIRI reconstruction is executed in a distributed, channel-wise fashion, together with an efficient large-scale RI measurement operator implementation ([Dabbech et al. 2025](#)). During initialisation, each process is assigned its channel's back-projected dirty image, local measurement operator, selected denoiser and initial spectral-index map. At each FB iteration (see Fig. 2(d)), gradient-descent and denoising steps then run concurrently across channels. Each channel process exchanges only its immediate neighbours' images to assemble the three-slice input cubes between these two steps, minimising communication overhead. As with the AIRI denoiser, the HyperAIRI denoiser has spatial faceting functionality. The denoisers can be applied on the overlapped facets extracted from $\hat{\mathbf{X}}_l^i$ in parallel. This hybrid spatial-spectral parallelisation scales nearly linearly with both the number of channels and available compute resources. As a result, our implementation delivers a highly efficient solver capable of handling large-scale hyperspectral datasets in practical runtimes.

5 VALIDATION ON SIMULATED VLA OBSERVATIONS

In this section, we study the performance of different algorithms for reconstructing hyperspectral RI image cubes from simulated observations.

5.1 Test dataset

The considered ground-truth images are derived from four radio images of size $N = 512 \times 512$, which consist of giant radio galaxies 3C 353 ([Swain et al. 1998](#)) and Messier 106 ([Shimwell et al. 2022](#)), and the radio galaxy clusters Abell 2034 and PSZ2 G165.68+44.01

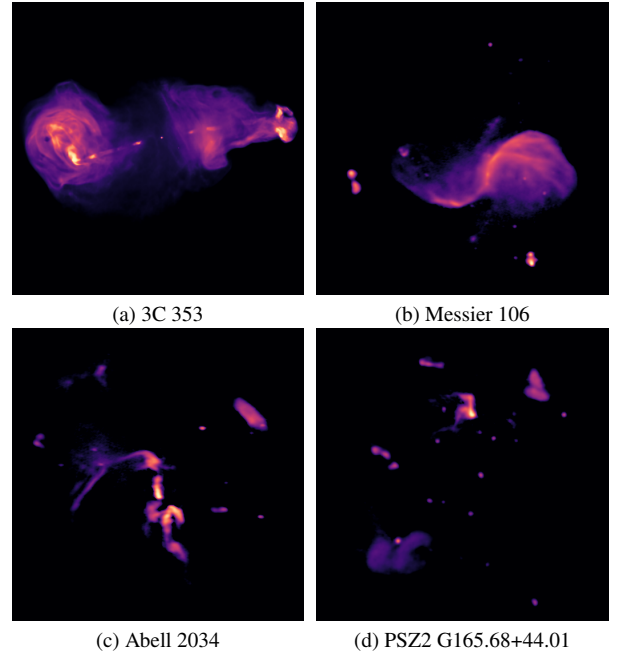


Figure 3. Original ground-truth images for generating the simulated test dataset. Each image has a size of 512×512 and the names of the sources are listed below the images.

([Botteon et al. 2022](#)) shown in Fig. 3. The images are first preprocessed to reduce noise and artefacts, then randomly exponentiated to make the final dynamic range in the interval $[10^3, 10^5]$. We follow the same preprocessing strategies for OAID and MRID and create 40 HDR monochromatic images. Following [Thouvenin et al. \(2023a\)](#), for each image, a spectral index map and a curvature map are generated, in a manner consistent with the procedure used for the training dataset. Specifically, the spectral index map is modelled as the sum of a blurred version of the ground truth in logarithmic scale and a Gaussian field, clipped to the range $[-5, 0]$. The curvature map is modelled as a Gaussian field, clipped to the range $[-0.5, 0.5]$. Each image cube contains $L = 36$ channels, with the first channel fixed at the observation frequency of 1 GHz and the last channel randomly chosen from the interval $[1.5, 2.0]$ GHz. The observation frequencies of the remaining channels are uniformly spaced within this range. We simulate 40 ground-truth image cubes of size $512 \times 512 \times 36$ following the spectral model (1).

Hyperspectral RI data are simulated using the antenna configurations of the VLA. The telescope is known for its unique ability to change the positions of the antennas along rail tracks, forming four standard configurations with maximum baselines ranging from 36.4 km to 1.03 km. Configurations with larger baselines provide higher angular resolution, while those with shorter baselines offer higher sensitivity to spatially extended emission. Astronomers often combine measurements from different configurations to obtain a comprehensive Fourier sampling of the target object. Under these considerations, we simulate RI observations combining configurations A and C of the VLA. The Fourier sampling patterns for both configurations are generated using the MeqTrees software package ([Noordam & Smirnov 2010](#)). We randomly vary the telescope's pointing direction, and the observation duration within the range $[5, 10]$ hours, and fix the integration time to 12 seconds. The resulting total number of points in each sampling pattern, at any given spectral channel, varies from 1.1×10^6 to 2.1×10^6 . Examples of simulated sampling patterns for spectral channels with different

Table 1. Numerical results of the various algorithms. Reconstruction quality of the image cube is reported in terms of SNR, SNR of the logarithmic scale image cubes (logSNR), residual-to-dirty ratio (RDR) and the SNR of the spectral index maps (sSNR). Computational performance details include the total number of iterations, the number of CPU cores and GPUs used in each run, the average timings for each reconstruction as well as for individual gradient (forward) and denoising (backward) steps. Values are presented in the format “average \pm standard deviation” except for computing resources. The average RDR of the ground truth images is $(2.46 \pm 1.37) \times 10^{-3}$. Note that for WSClean, the number of iterations indicates the number of major cycles.

Algorithm	Joint deconv.	SNR \pm std (dB)	logSNR \pm std (dB)	RDR \pm std ($\times 10^{-3}$)	sSNR \pm std (dB)	Iterations \pm std	Resources	t_{total} \pm std (hr)	t_{gradient} \pm std (s)	$t_{\text{denoising}}$ \pm std (s)	
						CPUs	GPUs				
uSARA	No	28.32 ± 3.24	21.17 ± 3.56	2.27 ± 1.32	9.54 ± 2.34	1251 ± 299	36	0	2.60 ± 0.55	2.10 ± 0.27	5.24 ± 6.73
AIRI	No	28.70 ± 2.36	20.67 ± 5.01	2.62 ± 1.41	9.18 ± 3.90	3000 ± 0	36	4	1.84 ± 0.14	1.60 ± 0.23	0.46 ± 0.32
WSClean	Yes	11.27 ± 1.57	12.05 ± 4.08	2.36 ± 1.27	3.81 ± 5.91	10 ± 1	36	0	0.56 ± 0.24	–	–
Hyper-uSARA	Yes	29.30 ± 2.91	22.30 ± 4.15	2.32 ± 1.34	11.35 ± 3.78	1827 ± 675	36	0	2.42 ± 0.87	2.09 ± 0.27	2.58 ± 1.43
HyperAIRI	Yes	30.53 ± 1.87	23.07 ± 5.13	2.44 ± 1.36	10.87 ± 3.91	3000 ± 0	36	4	1.90 ± 0.14	1.61 ± 0.23	0.52 ± 0.25

observation frequencies are shown in Fig. 1. The hyperspectral RI data are simulated under the assumption of a narrow field of view, and following (4), where the standard deviation of the observation noise is fixed across the spectral channels aligning with the target dynamic range of the cube as per the heuristic (14), such that the target dynamic range of the reconstructed image cube matches that of the corresponding ground-truth image cube. The observation’s nominal resolution is parametrised by the super-resolution factor, defined as the ratio between the image spatial Fourier bandwidth and the maximum projected baseline. We fix the super-resolution factor at the highest-frequency channel to 1.5, leading to a super-resolution factor across different channels in the range [1.5, 3.0]. The resulting test dataset is composed of 40 inverse problems.

5.2 Benchmark settings

For benchmarking, we compare HyperAIRI’s performance against four algorithms. These are its optimisation-counterpart Hyper-uSARA, the hyperspectral CLEAN variant in WSClean (Offringa & Smirnov 2017), and the monochromatic algorithms AIRI and uSARA which are applied for each channel independently. Briggs weighting with robustness parameter set to 0 is considered for all algorithms.

In our experiments, the regularisation parameters for the optimisation algorithms and the effective noise levels for PnP algorithms are directly linked to the heuristic noise level via (14) without further tuning. WSClean parameters are tuned on a small subset of the test dataset and then fixed across the entire dataset to ensure the best overall image quality. In particular, the auto-masking and auto-thresholding values are set to 1.0 and 0.5, respectively, and the number of polynomial terms for spectrum fitting is fixed at 4. The full WSClean command is shown in Appendix B. We also note that the WSClean reconstructions are normalised by the area of the CLEAN beam A_{beam} on a per-channel basis, thus converting the unit of pixel intensities from Jy/beam to Jy/pixel to align with the groundtruth image cube. The normalisation factor is given by

$$A_{\text{beam}} = \frac{\pi B_{\text{maj}} B_{\text{min}}}{4 \log 2} \quad (24)$$

where the respective B_{maj} and B_{min} are the size of the CLEAN restoring beam in the major and minor axes in the unit of pixel.

HyperAIRI, Hyper-uSARA, AIRI and uSARA are implemented in MATLAB, while WSClean is implemented in C++. All experiments were run on Cirrus, a UK Tier 2 HPC service that provides access to both CPU and GPU compute nodes. Each CPU node comprises two Intel 18-core Xeon E5-2695 processors with 256 GB of memory, while each GPU node comprises two 20-core Intel Xeon Gold 6148

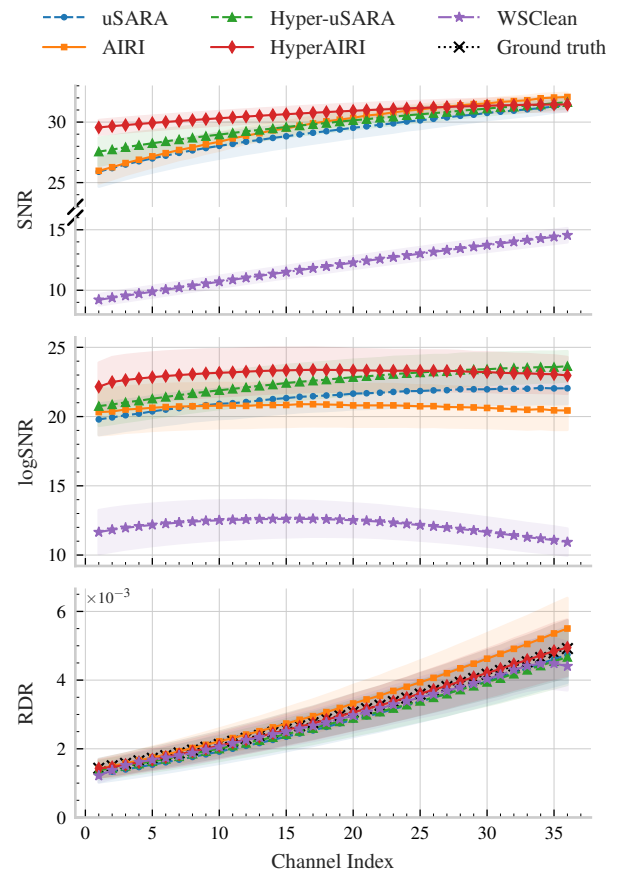


Figure 4. Channel-wise reconstruction metrics for various methods on the simulated test set. The channel index ranges from 1 to 36. From top to bottom, the panels show SNR, logSNR and RDR versus channel index, respectively. Each point represents the average metrics value for the corresponding channel index across all problems, and the shaded areas indicate the 95% confidence interval.

processors, four NVIDIA Tesla V100-SXM2-16GB GPUs, and 384 GB of memory. For each inverse problem in the test dataset, uSARA, WSClean and Hyper-uSARA run on a single CPU node, whereas AIRI and HyperAIRI were executed on a single GPU node to accelerate the inference of DNNs. Each AIRI and HyperAIRI denoisers is trained with half GPU node.

5.3 Evaluation metrics

To quantitatively compare the reconstruction quality of the various algorithms in terms of accuracy to the ground truth, we use two metrics. The first one is signal-to-noise (SNR) ratio. Given the ground truth $\bar{\mathbf{X}}$ and an estimate image cube \mathbf{X} , the SNR is calculated as

$$\text{SNR}(\mathbf{X}, \bar{\mathbf{X}}) = 20 \log_{10} \left(\frac{\|\bar{\mathbf{X}}\|_F}{\|\bar{\mathbf{X}} - \mathbf{X}\|_F} \right). \quad (25)$$

We also evaluate the SNR at each channel l which reads

$$\text{SNR}(\mathbf{x}_l, \bar{\mathbf{x}}_l) = 20 \log_{10} \left(\frac{\|\bar{\mathbf{x}}_l\|_2}{\|\bar{\mathbf{x}}_l - \mathbf{x}_l\|_2} \right). \quad (26)$$

To evaluate the algorithms' performance in reconstructing faint emissions, we evaluate the SNR on logarithmic scale images, denoted as logSNR. Given a ground-truth image cube, with a dynamic range a , we apply the logarithmic scale transform parametrised by a such that

$$\text{rlog}(\mathbf{X}) = \max(\mathbf{X}) \log_a \left(\frac{a}{\max(\mathbf{X})} \mathbf{X} + 1 \right), \quad (27)$$

where $\max(\cdot)$ extract the maximum pixel intensities in the input image cube. The overall and channel-wise SNRs are then computed on these logarithmically transformed image cubes with (25) and (26) as $\text{SNR}(\text{rlog}(\mathbf{X}), \text{rlog}(\bar{\mathbf{X}}))$ and $\text{SNR}((\text{rlog}(\mathbf{X}))_l, (\text{rlog}(\bar{\mathbf{X}}))_l)$, yielding the overall and channel-wise logSNR metrics respectively.

In assessing data fidelity in the image domain, we introduce the residual-to-dirty ratio (RDR). Consider the residual dirty image cube, defined as $\mathbf{X}^{\text{res}} = \mathbf{X}^{\text{dirty}} - \text{Re}\{\Phi^\dagger(\Phi(\mathbf{X}))\}$, the overall and channel-wise RDR values can be calculated as

$$\text{RDR}(\mathbf{X}^{\text{res}}, \mathbf{X}^{\text{dirty}}) = \|\mathbf{X}^{\text{res}}\|_F / \|\mathbf{X}^{\text{dirty}}\|_F \quad (28)$$

and

$$\text{RDR}(\mathbf{x}_l^{\text{res}}, \mathbf{x}_l^{\text{dirty}}) = \|\mathbf{x}_l^{\text{res}}\|_2 / \|\mathbf{x}_l^{\text{dirty}}\|_2 \quad (29)$$

respectively. If a reconstruction's RDR closely matches that of the corresponding ground-truth image, the reconstruction demonstrates high data fidelity.

Finally, the spectral index map from a given image cube \mathbf{X} , is obtained via linear regression applied at each pixel position to estimate the slope between the logarithm of spectral frequencies and the pixel intensities along the spectral axis following (23). To ensure numerical stability, the spectral index is only evaluated at pixels whose values above heuristic noise levels (14) across all the channels. Consider the groundtruth spectral index map $\bar{\alpha}$, the accuracy of the reconstructed spectral index map α is measured by the spectral-index SNR metric (sSNR), defined as $\text{SNR}(\alpha, \bar{\alpha})$.

5.4 Reconstruction results

Firstly, we discuss the overall numerical performance of the various methods on the simulated test dataset, as reported in Table 1, where metrics are computed over the entire image cubes. We also examine channel-wise metrics illustrated in Fig. 4, where each point represents the average across the test cases, and the shaded region denotes 95% confidence interval.

To analyse the fidelity of the reconstructed image cubes to the ground truth, we first examine the SNR metric quantifying how faithfully bright features are recovered. The hyperspectral algorithms Hyper-uSARA and HyperAIRI improve the mean SNR over their respective monochromatic counterparts uSARA and AIRI by about 1 and 1.5 dB. As expected, WSClean's reconstruction ranks

lowest, a consequence of smoothing with a channel-specific CLEAN beam and adding with the residual dirty image. Fig. 4 shows that, generally, channel-wise SNR obtained by all algorithms increases with the frequency. This behaviour could be explained by the nature of the hyperspectral Fourier sampling, where larger spatial bandwidths are probed at the highest frequencies. HyperAIRI exploits inter-channel correlations effectively, drastically narrowing the gap in SNR among the low and high frequencies. Similar behaviour is observed with Hyper-uSARA although to a lesser extent. We then examine the logSNR metric results, assessing the recovery of faint emissions, shows that Hyper-uSARA and HyperAIRI exceed their monochromatic counterparts in overall average logSNR by 1.1 and 2.4 dB respectively, with WSClean again lagging behind in quality. The channel-wise logSNR curves in Fig. 4 highlights the overall superior performance of HyperAIRI. Furthermore, we notice a consistent performance of the PnP approaches across channels, with a minor drop in the logSNR values at both ends, whereas the optimisation-based algorithms exhibit logSNR values increasing with the frequency. In contrast, WSClean displays more pronounced drops in logSNR at the lowest and highest frequencies.

Assessing reconstruction data consistency in the image domain via the RDR metric indicates that all methods achieve good performance, with average RDR values close to the ground-truth reference. uSARA falls slightly below the reference, suggesting minor overfitting, whereas AIRI lies just above, indicating slight under-fitting. Figure 4 shows that HyperAIRI's channel-specific RDR curve follows the ground truth across all channels. Overall, HyperAIRI provides the best data fidelity both in aggregate and on a per-channel basis.

We examine the spectral accuracy of the reconstructed images via the sSNR metric. The hyperspectral algorithms Hyper-uSARA and HyperAIRI improve over their monochromatic counterparts, confirming the benefit of exploiting spectral correlations. Specifically, Hyper-uSARA achieves the highest average sSNR, closely followed by HyperAIRI. The slightly lower sSNR achieved by the latter may be related to its relatively small receptive field in both spatial and spectral dimensions. In contrast, WSClean exhibits significantly lower sSNR, likely due to its inherent high-sensitivity to variations in spatial resolution across different channels.

Secondly, we conduct a qualitative analysis, by analysing the reconstructed images of a selected inverse problem, whose ground-truth cube is derived from the image of the radio galaxy 3C 353. Fig. 5 shows the reconstructions of the first and last channels obtained with different algorithms. The visual results are generally consistent with the quantitative analysis. By design, WSClean exhibits lower resolution and dynamic range. For the optimisation-based algorithms, Hyper-uSARA exhibits fewer wavelet-like artefacts around the edges of bright structures than its monochromatic counterpart (see the two zoom regions), particularly in the first channel. As for the PnP algorithms, they both exhibit fewer ringing artefacts than uSARA and Hyper-uSARA, especially around the central black hole and the bright emission in the top-right zoom. Furthermore, HyperAIRI produces sharper depiction of relatively bright structures. For instance, the central point source is more compact in the HyperAIRI reconstruction, with a more homogeneous radius across spectral channels. However, compared to Hyper-uSARA, HyperAIRI appears to capture a smooth depiction of the faint extended emission whose intensity values are 3 to 4 orders of magnitude lower than the peak pixel value. This trend, particularly noticeable at the highest frequency, is also reflected in the channel-wise logSNR metric. This could be due to the effective noise level and the resulting choice of the denoiser.

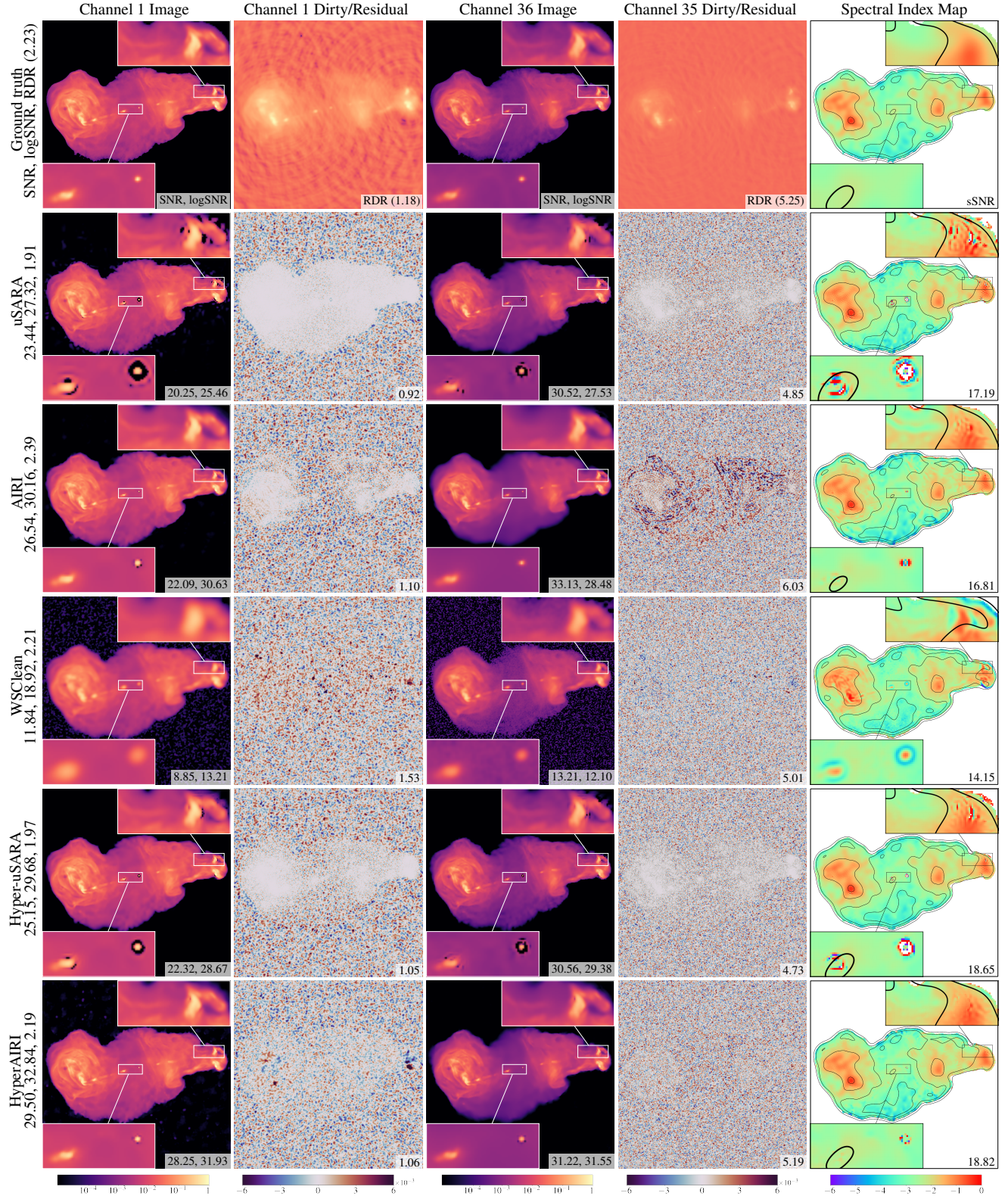


Figure 5. Reconstruction results of a simulated inverse problem using radio galaxy image of 3C 353. Row 1 shows the ground truth. Row 2-6 show results from uSARA, AIRI, WSClean, Hyper-uSARA, and HyperAIRI. Columns 1 and 3 display estimated images at the first and last channels in a logarithmic scale. Columns 2 and 4 display the back-projected dirty images (row 1, normalized to $[0, 1]$) or the back-projected residual images (rows 2-6). Column 5 illustrates the spectral index maps. Two zoomed-in regions, one focusing on the central black hole and the other on a hotspot to the right, highlight visual differences. Channel-wise SNR and logSNR values (dB) are indicated at the bottom-right corners of panels in columns 1 and 3, RDR values (10^{-3}) in columns 2 and 4 (with ground-truth values in row 1), and sSNR values (dB) in columns 5. Overall metrics for the entire image cube are listed next to each algorithm name, with units matching with the channel-wise metrics. The ground-truth overall RDR value is included in the top-left bracket of row 1.

Lowering the heuristic noise level in the highest-frequency channel may help restore those faint features in this case.

The inspection of the residual dirty images shows that WSClean exhibits good data fidelity in the image domain, with the signature of the radio emission being hardly noticeable. As for Hyper-uSARA, while improving over its monochromatic counterpart, still shows signs of data over-fitting. Finally, HyperAIRI achieves comparable data fidelity to that of WSClean. Its residual dirty images are generally homogeneous, particularly in comparison to AIRI, apart from some residual structure in the first channel at the pixel positions of the two hotspots.

The spectral index maps produced by all methods generally agree with the ground truth. Upon closer inspection, the spectral index maps of WSClean exhibit fake details which strongly correlate with image spatial features (see the two zooms). This effect arises from CLEAN’s high sensitivity to the varying spatial resolution across channels. In contrast, the spectral index map of both Hyper-uSARA and HyperAIRI are more faithful to the ground truth, with both algorithms substantially reducing the artefacts present in their monochromatic counterparts. When comparing these two hyperspectral algorithms, the spectral index maps of HyperAIRI shows even milder ringing artefacts (see the zooms of the central black hole and the right hotspot) but appears marginally more grainy in the bottom region, which is linked to the smoothness of its reconstruction in the higher-frequency channels.

The computational details of various algorithms are indicated in Table 1. As expected, WSClean appears to be 5 and 4 times faster than optimisation algorithms and PnP algorithms respectively. Its computational efficiency is explained by its small number of passes through the measurement operators within its major cycle. In comparison, the rest of the algorithms, sharing the same iterative structure, are highly iterative in nature. On average, both optimisation-based algorithms require comparable computational time, despite Hyper-uSARA demanding nearly 50% more iterations than uSARA. This highlights the efficiency of the hyperspectral regularisation, whose sub-iterative proximity operator converges at least twice as fast. PnP algorithms also exhibit comparable computational time. Although HyperAIRI denoisers are more complex than AIRI, they do not introduce additional computational cost. Notably, PnP approaches generally require more iterations than pure optimisation methods. Nevertheless, they remain faster overall due to the efficient GPU-based inference of their DNN denoisers. In addition, the gradient steps of the PnP algorithms are slightly faster than those of the optimisation-based algorithms, primarily because of differences in CPU performance and memory configuration between the CPU and GPU nodes on Cirrus.

6 VALIDATION ON REAL ASKAP OBSERVATIONS

In this section, we revisit the ASKAP measurements of the field SB9442-35 previously imaged by Wilber et al. (2023a,b) with uSARA and AIRI. To evaluate the performance of proposed hyperspectral algorithms, Hyper-uSARA and HyperAIRI, we support our analysis with the reconstructions obtained by their monochromatic counterparts, as well as the hyperspectral CLEAN variant in WSClean.

6.1 Data details for the field SB9442-35

The hyperspectral measurements used in this experiment are part of the ASKAP EMU Pilot Survey (Norris et al. 2021). In this survey, each Scheduling Block (SB) provides 36 different measurement sets,

each corresponding to a different primary beam. For the real data experiment, we select the measurement set of Beam 35 of SB9442, centred at the radio source PKS 2130-538 of the galaxy cluster Abell 3785, known as the “dancing ghosts”. The observation spans 10 hours covering the frequency band 800-1088 MHz with a frequency step size of 1 MHz, yielding 288 spectral channels. The selected hyperspectral measurements were calibrated with the ASKAPsoft (Hotan et al. 2021) and are accessible through the CSIRO ASKAP Science Data Archive (Chapman et al. 2015).

6.2 Imaging settings

Following the imaging considerations of Wilber et al. (2023a,b), the measurement set is divided into 8 spectral windows, combining 36 channels each. The visibilities in each spectral window are concatenated together during imaging. The target image cube thus contains 8 spectral channels. Each channel has a pixel size of 4096×4096 and a cell size of 2.20 arcsec, achieving a final FoV of $2.57^\circ \times 2.57^\circ$, corresponding to a super-resolution factor of 2.22 at the highest-frequency channel and 2.91 at the lowest-frequency channel. The w -correction is enabled for all algorithms to account for w -effect in wide-field imaging. Briggs weighting with the robustness parameter fixed to -0.25 is considered.

The choices of algorithm-specific parameters are detailed below. For WSClean, we enable the joint-channel deconvolution and consider 4 polynomial terms for spectral fitting. The w -griddler is selected for gridding and w -correction. The remaining parameters are set consistent with the considerations of Wilber et al. (2023a), and the full WSClean command is shown in Appendix B. For comparison, the WSClean image cube is normalised channel-wise by the flux of the corresponding restoring beam as per (24). The regularisation parameter λ in uSARA- $\ell_{2,1}$ and the effective noise level for the denoisers in HyperAIRI are adjusted to 0.3 and 0.5 times the heuristic noise level (14) respectively. This adjustment improves the overall imaging quality while mitigating calibration artefacts. The MATLAB-based measurement operator encapsulates a hybrid w -projection w -stacking approach to correct for the w -effect (Dabbech et al. 2022, 2025).

To evaluate the spectral index maps from the reconstructed image cubes, we follow the considerations of Wilber et al. (2023a,b). For each image cube, a smoothing Gaussian kernel was applied, with a full width at half maximum (FWHM) of 20 arcsec for WSClean and 5 arcsec for the remaining algorithms. Subsequently, the logarithm of the pixel intensities of these channels are fitted to a linear function with the slope to be the spectral index map, as shown in (23).

All experiments were run on the Cirrus HPC systems. For WSClean, 1 full CPU node is allocated. For Hyper-uSARA, 4 CPU nodes are assigned with 142 cores are used during reconstruction. Meanwhile, HyperAIRI ran on 4 GPU nodes, where 142 CPU cores and 8 GPUs are used.

6.3 Reconstruction results

We examine the reconstructions provided by the different algorithms in Fig. 6-8, at both lowest (left panels) and highest (right panels) frequencies. Fig. 6 exhibits AIRI (top panels) and uSARA (bottom panels) images from Wilber et al. (2023b,a). Fig. 7 presents WSClean images. Fig. 8 displays HyperAIRI (top panels) and Hyper-uSARA (bottom panels) images. In each panel, we consider zooms on eight selected regions as follows: region (i) centred at the “dancing ghosts”; regions (ii) and (iv) corresponding to areas containing both extended

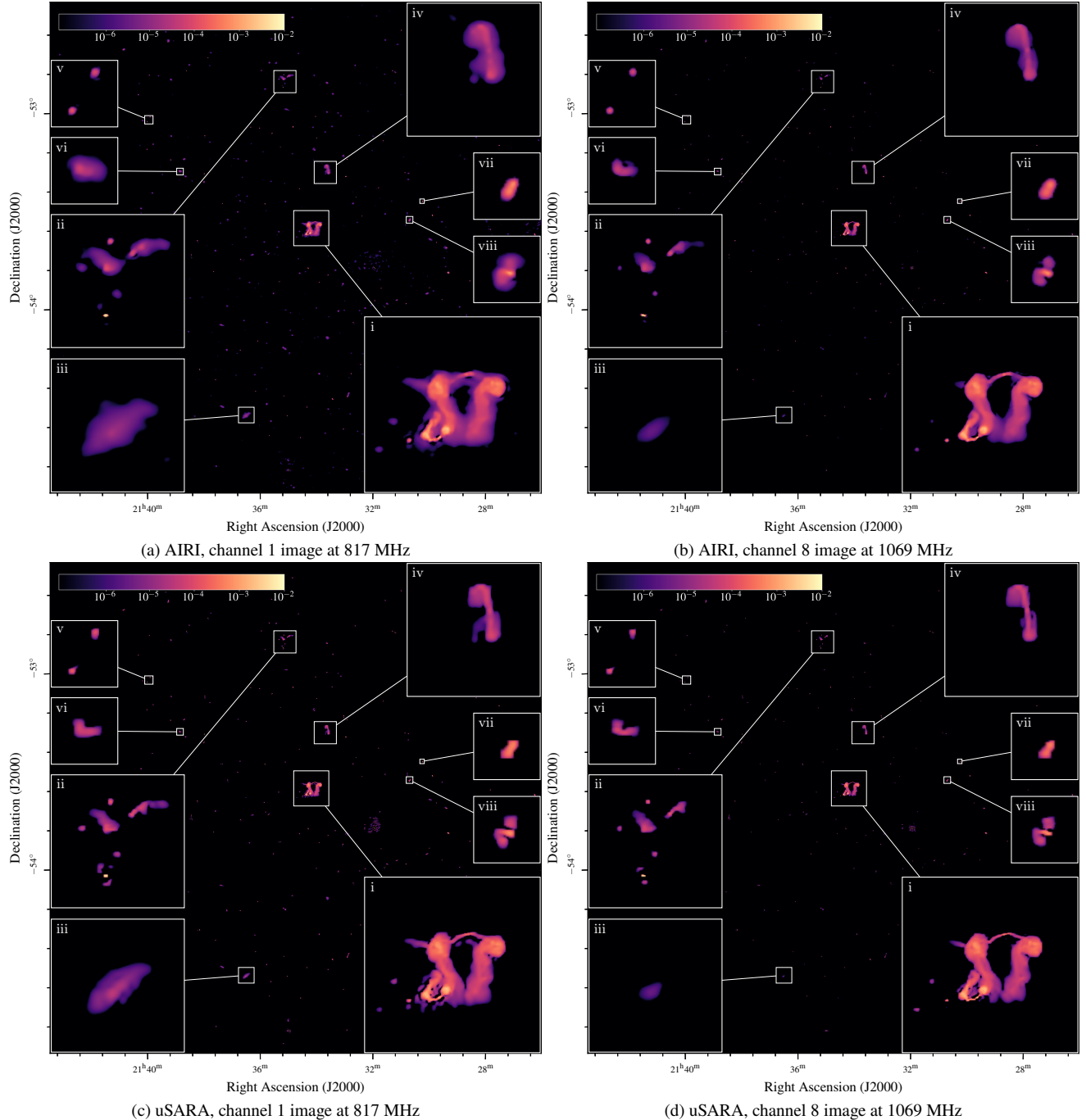


Figure 6. Reconstructed images of the field SB9442-35 at the frequencies 817 MHz (left) and 1069 MHz (right), obtained using the monochromatic algorithms AIRI (top), and uSARA (bottom) (Wilber et al. 2023b,a). Each panel is overlaid with zooms on selected regions: zoom (i) is centred on the “dancing ghosts”; zooms (ii) and (iv) show regions with both extended and compact radio sources; zoom (iii) contains the star-forming galaxy NGC 7090; zooms (v)-(viii) focus on 4 compact sources.

and compact radio sources; region (iii) centred on the star-forming galaxy NGC 7090; and regions (v)-(viii) centred on compact sources with varying morphologies.

Compared with their monochromatic counterparts, the proposed hyperspectral algorithms recover significantly more faint background sources, capture finer details of the radio emission, and exhibit improved inter-channel consistency. Among the hyperspectral approaches, HyperAIRI achieves distinguished source sharpness and recovers the largest number of compact sources, albeit with some

noise-like residual patterns suggesting some extent of data overfitting. On the other hand, Hyper-uSARA fails to capture some of the faint compact background sources due to its joint sparsity regularisation, enforcing pixel values of sources, detected in some channels only, to be set to zero. WSClean reconstructions are smoother by design, with some faint sources appear to be buried in the noise. While one could further optimise the noise-level scaling factors on a per-channel basis as in Wilber et al. (2023a,b) or consider per-channel visibility calibration to better balance background residuals against

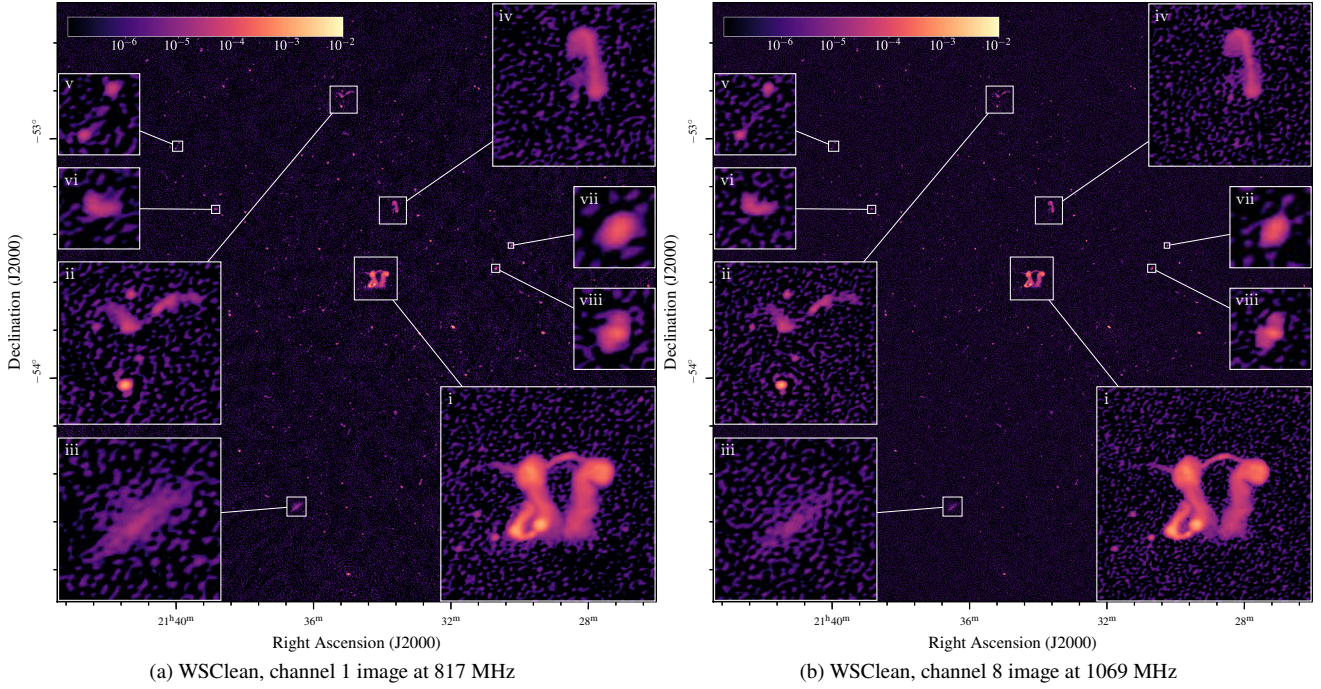


Figure 7. Reconstructed images of the field SB9442-35 at the frequencies 817 MHz (left) and 1069 MHz (right), obtained using the WSClean with joint-channel deconvolution. The zoom regions are identical to those in Fig. 6.

source recovery, these processing strategies lie beyond the scope of this experiment.

A detailed examination of the zoom regions highlights substantial differences in the imaging precision of the different algorithms in terms of angular resolution, dynamic range and the ability to capture faint emission, and spectral correlation. Firstly, the superior angular resolution achieved by HyperAIRI at both channels compared to the benchmark is exemplified by zoom regions (vi), (vii) and (viii), with Hyper-uSARA ranking second. Both algorithms reveal inner cores and jets of the selected radio galaxies, whereas their monochromatic counterparts and even WSClean provide a blurred depiction of the same sources. Notably, HyperAIRI resolves the inner core of the radio galaxy in region (vi), and distinctly separates the two compact sources at the centre of region (viii). Secondly, the enhanced sensitivity and dynamic-range of the proposed hyperspectral algorithms is showcased in zoom region (v). Both HyperAIRI and Hyper-uSARA successfully recover the faint jets emanating from the two hotspots. The faint features are completely absent in the monochromatic reconstructions, and are not revealed clearly in WSClean’s images. Thirdly, consistency of spectral behaviour achieved by the proposed hyperspectral algorithms is exemplified by the V-shaped emission in region (ii), the star-forming galaxy NGC 7090 in region (iii), and the two-sided jet emission and nearby point sources in region (iv), with faint structures preserved across channels. Examining region (iii) at the highest frequency, monochromatic algorithms fail to recover NGC 7090’s fusiform morphology. For WSClean, the source is buried in the noise. By contrast, both HyperAIRI and Hyper-uSARA reliably restore NGC 7090’s elongated form, with the former providing a clearer depiction of the diffuse emission.

In what follows, we provide a deeper analysis of the recovery of the “dancing ghosts” in zoom region (i), including data fidelity and the source’s spectral index map. The source is the most prominent in this field, notable for its complex morphology. It comprises the emission of two active galactic nuclei (AGN): the first

(WISEA J213406.70–533418.7) at the centre of the north bridge, and the second (WISEA J213417.69–533811.1) in the southeast filament (Norris et al. 2021; Velović et al. 2023). All hyperspectral algorithms provide consistent reconstructions across channels. In particular, two jets from the two lobes of the first AGN respectively pointing towards the northeast exhibit similar shapes in both the first and last channels. Hyper-uSARA offers sharper edges and lower background noise, albeit with minor wavelets artefacts around the jets and lobes of the second AGN. HyperAIRI tends to deliver slightly higher resolution and recover more of the neighbouring compact point-like sources than Hyper-uSARA. However, the PnP algorithm seems to depict the north bridge with a chain of dots, which is likely a reconstruction artefact. This could be indicative of training dataset bias, with half of the images simulated from optical astronomical images dominated by point-like sources. For insight into the achieved data fidelity, residual dirty images associated with zoom region (i) are shown in Fig. 9. The hyperspectral algorithms deliver noise-like residuals, enabling improved data fidelity over monochromatic algorithms. Unlike HyperAIRI and WSClean, the signature of the “dancing ghosts” is somewhat visible in the residual dirty image of Hyper-uSARA, suggesting a minor data over-fitting. The source’s spectral index maps are shown in Fig. 10. Hyperspectral algorithms yield smaller and more physically plausible spectral index values, while uSARA and AIRI show moderately higher values likely due to spectral inconsistency across channels. This is exemplified by the filaments associated with the two AGN and in their associated lobes.

Finally, the computational performance of the hyperspectral algorithms varies considerably due to the algorithmic and implementation differences. WSClean completes the reconstruction in 2.07 hours, making it the fastest. HyperAIRI requires 12.16 hours and runs 2500 iterations in FB, while Hyper-uSARA is the slowest, taking 24.48 hours to finish 1764 iterations in FB. Notably, the denoising (backward) step in Hyper-uSARA averages 35.13 seconds per iteration, compared to only 5.35 seconds for HyperAIRI. This difference is

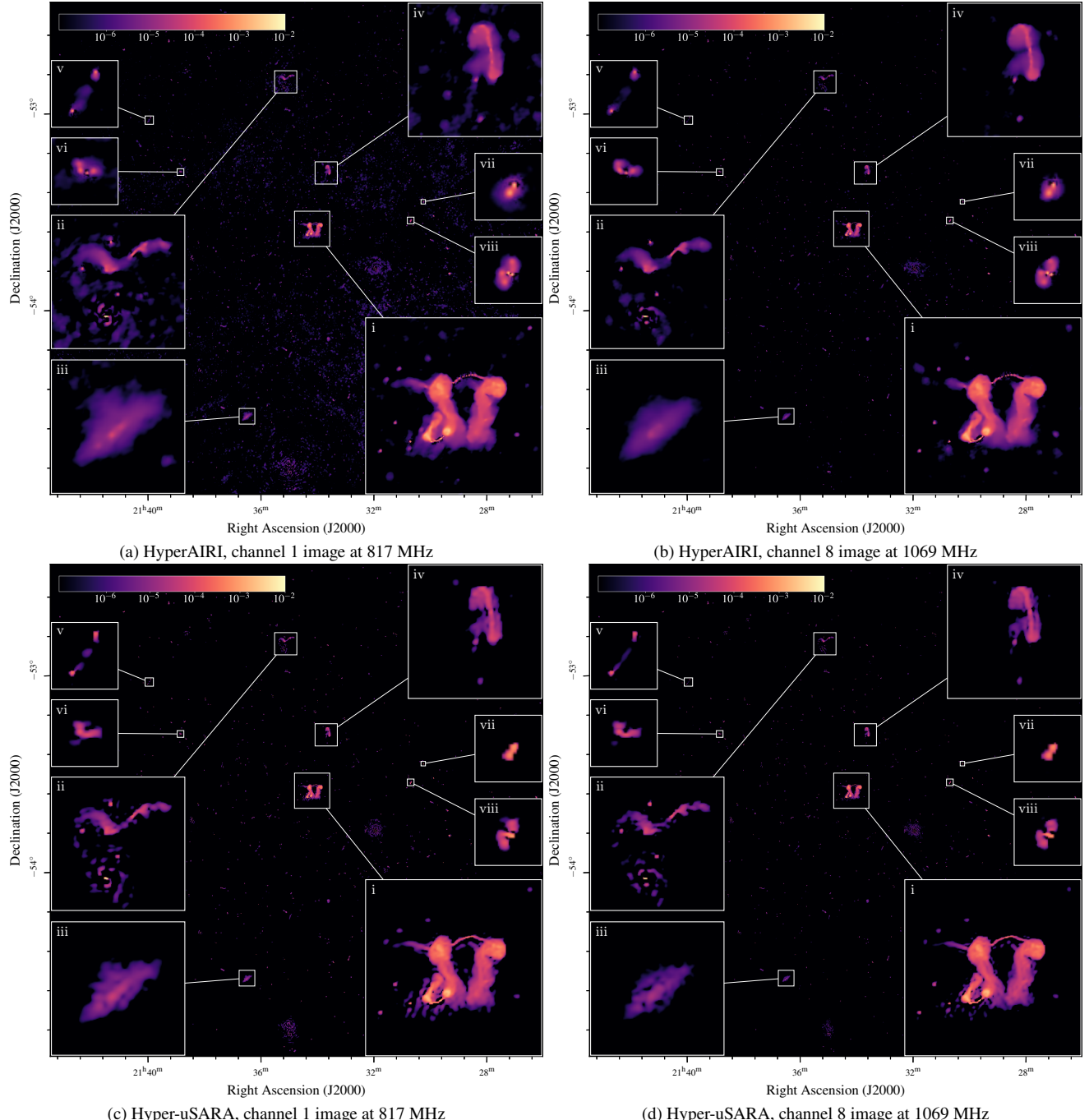


Figure 8. Reconstructed images of the field SB9442-35 at the frequencies 817 MHz (left) and 1069 MHz (right), obtained using the HyperAIRI (top) and Hyper-uSARA (bottom). The zoom regions are identical to those in Fig. 6.

primarily due to the sub-iterative nature of the SARA- $\ell_{2,1}$ proximity operator and additional overhead from global gathering and scattering of wavelet coefficients for each channel during its denoising steps.

7 CONCLUSIONS

In this paper, we have introduced HyperAIRI, a novel PnP algorithm for extreme-scale hyperspectral RI imaging. HyperAIRI builds on the monochromatic FB-PnP algorithm AIRI, adapting its DNN de-

noisers to process hyperspectral RI image cubes, thereby exploiting their inherent spectral correlations. We also formally introduce the optimisation-based counterpart algorithm, Hyper-uSARA, which adopts the same FB iterative structure. Moreover, Hyper-uSARA can be interpreted as a simplified variant of HyperSARA (Abdulaziz et al. 2019; Thouvenin et al. 2023a), benefiting from an unconstrained formulation of the minimisation task, thus eliminating the need for exact prior knowledge of the RI noise level.

HyperAIRI denoisers take as input adjacent spectral channels to capture local correlations, while simultaneously injecting a power-law spectral model that facilitates the propagation of global spectral

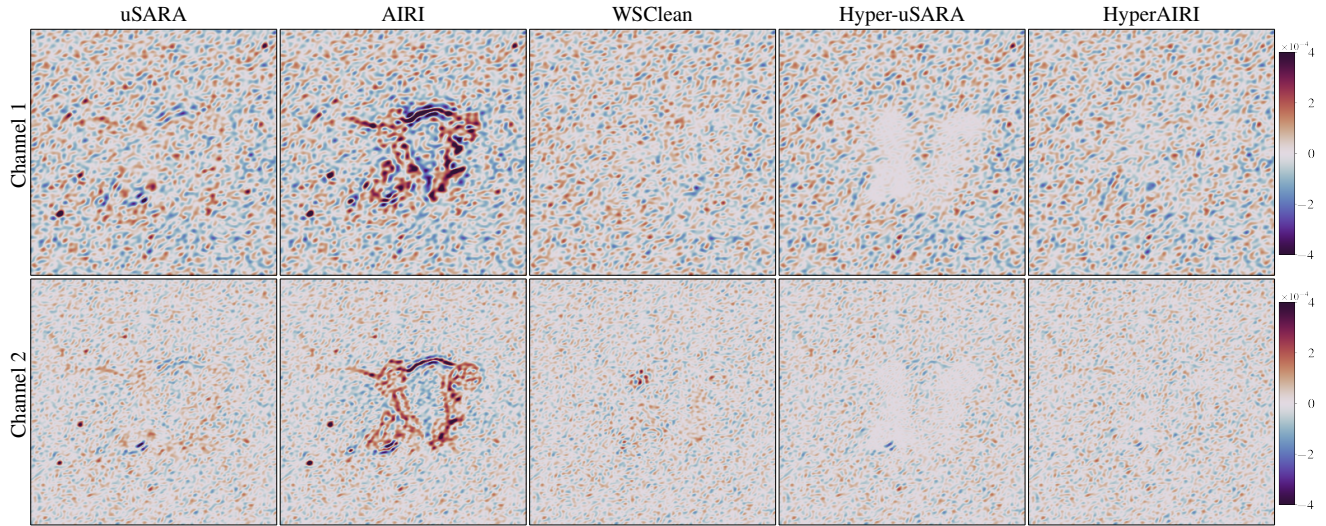


Figure 9. Residual dirty images zoomed at the “dancing ghosts”, for channel 1 (top row) and 8 (bottom row) from the reconstructions produced by the algorithms shown in Figs. 6-8

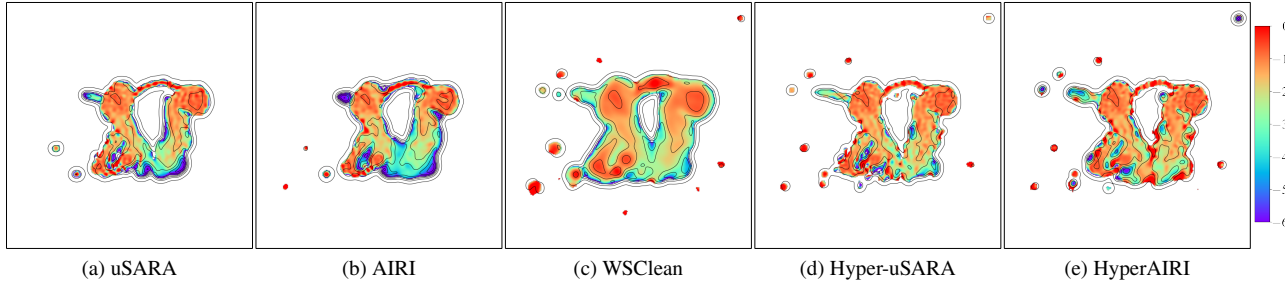


Figure 10. The spectral index maps of the “dancing ghosts” evaluated from the reconstructions of different algorithms. Panels (a) and (b) are extracted from the reconstructions of Wilber et al. (2023a,b). The maps are computed after convolving channel images with a Gaussian beam of 20 arcsec for WSClean and 5 arcsec for the other reconstructions.

information across channels. This design reduces the need for global communications, thereby improving computational efficiency during both training and image reconstruction, while maintaining precision imaging. Furthermore, HyperAIRI denoisers adapt easily to any image cube size through its flexible spatial-spectral faceting. Inheriting from AIRI its training strategy, which is fully decoupled from the measurement process, HyperAIRI denoisers can be applied under varying observational setup without the need for retraining. HyperAIRI also benefits from convergence guarantees owing to its non-expensive denoisers. The resulting precision, flexibility and scalability mark a significant improvement over the state-of-the-art methods, so far struggling to achieve these requirements simultaneously.

These strengths of HyperAIRI are reflected in our experimental results both in simulation and on real observations. On simulated observations, it delivers substantial improvements in quantitative metrics, visual quality, data consistency, and spectral coherence compared with the monochromatic algorithms, AIRI and uSARA, as well as CLEAN with joint-channel deconvolution in WSClean. Results from real ASKAP observations further confirm the applicability of HyperAIRI in large-scale measurements. Compared with other methods, HyperAIRI is able to capture faint emissions, improve resolution, and enhance spectral correlation while maintaining high data fidelity.

Despite its promise for precision hyperspectral imaging, HyperAIRI remains computationally expensive due to the highly iterative nature of the underpinning FB, in which frequent calls of the

measurement operator dominate the overall runtime. Inspired by CLEAN-based algorithms, exploring a major-minor cycle algorithmic structure with PSF approximations of the measurement operators inside minor cycles is a potential solution to reduce the computational cost. Additionally, building on the initial attempts in small-scale cases (Aghabiglou et al. 2025), developing a fully GPU-based implementation tailored for extreme-scale problems can significantly bridge the computational gap with WSClean.

Beyond scalability, further gains in reconstruction quality could be achieved. In particular, exploring advanced denoiser architectures that incorporate self- and cross-attention mechanisms (Vaswani et al. 2017), to exploit non-local features across the spatial and spectral domains, could enhance HyperAIRI’s precision. Endowing HyperAIRI with a calibration functionality is also crucial to ensure the high-precision imaging required for high-sensitivity observations from next-generation telescopes.

ACKNOWLEDGEMENTS

This research was supported by UK Research and Innovation through the EPSRC grant EP/T028270/1, and the STFC grants ST/W000970/1 and APP31234. The research used Cirrus, a UK National Tier-2 HPC Service at EPCC funded by the University of Edinburgh and EPSRC (EP/P020267/1). ASKAP, from which the data under scrutiny originate, is part of the Australia Telescope Na-

tional Facility managed by CSIRO. This project used public archival data from the Dark Energy Survey (DES).

DATA AVAILABILITY

HyperAIRI DNNs are available on the [Heriot-Watt University research portal](#). The images used to generate training datasets are sourced as follows. Optical astronomy images are gathered from NOIRLab/NSF/AURA/H.Schweiker/WIYN/T.A.Rector (University of Alaska Anchorage). Medical images are obtained from the NYU fastMRI Initiative database ([Zbontar et al. 2018](#); [Knoll et al. 2020](#)). The RI images used to build the simulated test dataset come from NRAO Archives, LOFAR HBA Virgo cluster survey ([Edler et al. 2023](#)), and LoTSS-DR2 survey ([Shimwell et al. 2022](#)). The ASKAP data underlying this article (calibrated visibilities and mosaic images of Scheduling Blocks) are made publicly available for viewing and downloading at [CSIRO ASKAP Science Data Archive](#) (CASDA, [Chapman et al. 2015](#)), and can be accessed with the unique Project Identifiers AS101. The uSARA and AIRI reconstructions of ASKAP used for comparison can be found through the DOI [10.17861/5a60f25b-d43b-4807-ba02-a69bc460db03](#).

REFERENCES

Abdulaziz A., Dabbech A., Onose A., Wiaux Y., 2016, in EUSIPCO. pp 388–392

Abdulaziz A., Dabbech A., Wiaux Y., 2019, MNRAS, 489, 1230

Aghabiglou A., San Chu C., Dabbech A., Wiaux Y., 2024, ApJS, 273, 3

Aghabiglou A., Chu C. S., Tang C., Dabbech A., Wiaux Y., 2025, ApJS, 280, 63

Arras P., Bester H. L., Perley R. A., Leike R., Smirnov O., Westermann R., Enßlin T. A., 2021, A&A, 646, A84

Bauschke H. H., Combettes P. L., Bauschke H. H., Combettes P. L., 2017, Convex analysis and monotone operator theory in Hilbert spaces. Springer

Birdi J., Repetti A., Wiaux Y., 2018, MNRAS, 478, 4442

Botteon A., et al., 2022, A&A, 660, A78

Carrillo R. E., McEwen J. D., Wiaux Y., 2012, MNRAS, 426, 1223

Ceccotti E., et al., 2023, MNRAS, 525, 3946

Chapman J., Dempsey J., Miller D., Pritchard J., Sangster E., Whiting M., Dart M., 2015, IAU Gen. Assem., 22, 2232458

Combettes P. L., Pesquet J.-C., 2011, in Bauschke H. H., Burachik R. S., Combettes P. L., Elser V., Luke D. R., Wolkowicz H., eds., Fixed-Point Algorithms for Inverse Problems in Science and Engineering. Springer, pp 185–212

Condat L., 2013, J. Optim. Theory Appl., 158, 460

Connor L., Bouman K. L., Ravi V., Hallinan G., 2022, MNRAS, 514, 2614

Cornwell T. J., 2008, IEEE J. Sel. Top. Signal Process., 2, 793

Dabbech A., Wolz L., Pratley L., McEwen J. D., Wiaux Y., 2017, MNRAS, 471, 4300

Dabbech A., Onose A., Abdulaziz A., Perley R. A., Smirnov O. M., Wiaux Y., 2018, MNRAS, 476, 2853

Dabbech A., Terris M., Jackson A., Ramatsoku M., Smirnov O. M., Wiaux Y., 2022, ApJ, 939, L4

Dabbech A., Aghabiglou A., San Chu C., Wiaux Y., 2024, ApJ, 966, L34

Dabbech A., Jackson A., Wiaux Y., 2025, In Prep.

De Gasperin F., Intema H., Frail D., 2018, MNRAS, 474, 5008

Drozdova M., et al., 2024, A&A, 683, A105

Edler H., et al., 2023, A&A, 676, A24

Fessler J. A., Sutton B. P., 2003, IEEE Trans. Signal Process., 51, 560

Gheller C., Vazza F., 2022, MNRAS, 509, 990

Goodfellow I. J., Shlens J., Szegedy C., 2014, arXiv preprint arXiv:1412.6572

Högblom J., 1974, A&AS, 15, 417

Hotan A., et al., 2021, Publ. Astron. Soc. Aust., 38, e009

Jonas J. L., 2009, Proc. IEEE, 97, 1522

Junklewitz H., Bell M., Enßlin T., 2015, A&A, 581, A59

Junklewitz H., Bell M., Selig M., Enßlin T., 2016, A&A, 586, A76

Kingma D. P., Ba J., 2014, arXiv preprint arXiv:1412.6980

Knoll F., et al., 2020, Radiol. Artif. Intell., 2, e190007

Monga V., Li Y., Eldar Y. C., 2021, IEEE Signal Process. Mag., 38, 18

Nguyen A., Yosinski J., Clune J., 2015, in Proc. IEEE Conf. Comput. Vis. Pattern Recognit.. pp 427–436

Noordam J. E., Smirnov O. M., 2010, A&A, 524, A61

Norris R. P., et al., 2021, Publ. Astron. Soc. Aust., 38, e046

Offringa A., Smirnov O., 2017, MNRAS, 471, 301

Onose A., Carrillo R. E., Repetti A., McEwen J. D., Thiran J.-P., Pesquet J.-C., Wiaux Y., 2016, MNRAS, 462, 4314

Onose A., Dabbech A., Wiaux Y., 2017, MNRAS, 469, 938

Pang T., Du C., Dong Y., Zhu J., 2018, Adv. Neural Inf. Process. Syst., 31

Perley R., Chandler C., Butler B., Wrobel J., 2011, The Astrophysical Journal Letters, 739, L1

Pesquet J.-C., Repetti A., Terris M., Wiaux Y., 2021, SIAM J. Imaging Sci., 14, 1206

Pratley L., McEwen J. D., d'Avezac M., Carrillo R. E., Onose A., Wiaux Y., 2018, MNRAS, 473, 1038

Rau U., Cornwell T. J., 2011, A&A, 532, A71

Reehorst E. T., Schniter P., 2018, IEEE Trans. Comput. Imaging, 5, 52

Repetti A., Wiaux Y., 2021, SIAM J. Optim., 31, 1215

Repetti A., Birdi J., Dabbech A., Wiaux Y., 2017, MNRAS, 470, 3981

Romano Y., Elad M., Milanfar P., 2017, SIAM J. Imaging Sci., 10, 1804

Roth J., Arras P., Reinecke M., Perley R. A., Westermann R., Enßlin T. A., 2023, A&A, 678, A177

Sault R., Wieringa M., 1994, A&AS, 108, 585

Scaife A. M. M., 2020, Philos. Trans. R. Soc. A, 378, 20190060

Scaife A. M., Heald G. H., 2012, MNRAS, 423, L30

Shimwell T., et al., 2022, A&A, 659, A1

Swain M. R., Bridle A. H., Baum S. A., 1998, ApJ, 507, L29

Terris M., Abdulaziz A., Dabbech A., Jiang M., Repetti A., Pesquet J.-C., Wiaux Y., 2019, in Proc. Signal Process. Adapt. Sparse Struct. Represent. Workshop.

Terris M., Dabbech A., Tang C., Wiaux Y., 2023, MNRAS, 518, 604

Terris M., Tang C., Jackson A., Wiaux Y., 2025, MNRAS, 537, 1608

Thompson A. R., Moran J. M., Swenson G. W., 2017, Interferometry and Synthesis in Radio Astronomy. Springer Nature

Thouvenin P.-A., Abdulaziz A., Dabbech A., Repetti A., Wiaux Y., 2023a, MNRAS, 521, 1

Thouvenin P.-A., Dabbech A., Jiang M., Abdulaziz A., Thiran J.-P., Jackson A., Wiaux Y., 2023b, MNRAS, 521, 20

Vaswani A., Shazeer N., Parmar N., Uszkoreit J., Jones L., Gomez A. N., Kaiser L., Polosukhin I., 2017, Adv. Neural Inf. Process. Syst., 30

Velović V., Cotton W. D., Filipović M. D., Norris R. P., Barnes L. A., Condon J. J., 2023, MNRAS, 523, 1933

Venkatakrishnan S. V., Bouman C. A., Wohlbeg B., 2013, in Proc. IEEE Glob. Conf. Signal Inf. Process.. pp 945–948

Vijay Kartik S., Carrillo R. E., Thiran J.-P., Wiaux Y., 2017, MNRAS, 468, 2382

Wang R., Chen Z., Luo Q., Wang F., 2023, in ECAI. pp 2499–2506

Wilber A. G., Dabbech A., Jackson A., Wiaux Y., 2023a, MNRAS, 522, 5558

Wilber A. G., Dabbech A., Terris M., Jackson A., Wiaux Y., 2023b, MNRAS, 522, 5576

Zbontar J., et al., 2018, arXiv preprint arXiv:1811.08839

APPENDIX A: NOTATION LIST

A list of mathematical notations used in this paper is listed in Table A1.

Table A1. Essential mathematical notations

$(\cdot)_l$	Choose l -th column from the input matrix
$\ \cdot\ _1, \ \cdot\ _2$	ℓ_1 and ℓ_2 norm
$\ \cdot\ _F$	Frobenius norm
$\ \cdot\ _S$	Spectral norm
$\iota_C(\cdot)$	Indicator function of set C
$\text{prox}_r(\cdot)$	Proximity operator for function $r(\cdot)$
$D(\cdot)$	Denoiser
$\Phi(\cdot), \Phi^\dagger(\cdot)$	Forward and adjoint measurement operator for hyperspectral image cube
M	Number of visibilities in each channel
N	Number of pixels in the image of each channel
L	Total number of channels
b	Number of wavelet bases for the redundant wavelet dictionary
Φ_l, Φ_l^\dagger	Forward and adjoint measurement operator at channel l
$\mathbf{X} = ([\mathbf{x}_l]_{1 \leq l \leq L})$	Hyperspectral image cube
$\mathbf{\tilde{X}}$	Ground truth image cube
$\mathbf{X}^{\text{dirty}}$	Dirty image cube
\mathbf{X}^{res}	Residual dirty image cube
$\mathbf{Y} = ([\mathbf{y}_l]_{1 \leq l \leq L})$	Hyperspectral measurements
$\mathbf{N} = ([\mathbf{n}_l]_{1 \leq l \leq L})$	Hyperspectral measurements noise
τ_l	Standard deviation of \mathbf{n}_l
ν_l	Spectral frequency of channel l
$\check{\nu}_l = (\check{\nu}_{l-1,l}, \check{\nu}_{l+1,l})$	The frequency ratios between ν_{l-1} , ν_{l+1} and ν_l respectively
α, β	Spectral index map and spectral curvature map
$\tilde{\alpha}$	Estimated spectral index map
$\sigma_{\text{heu},l}$	Heuristic noise level in the image domain of channel l
ρ_l	Maximum pixel intensity of image in channel l
Ψ^\dagger, Ψ	Redundant wavelet dictionary and its adjoint transform
λ	The regularisation parameter in the objective function
γ	The step size for the gradient descent
ϵ	The estimated noise floor level in the wavelet coefficients

```
-no-min-grid-resolution -auto-threshold 1.0 \
-automatic-mask 2.5 -mgain 0.8 -fit-beam -pol i \
-niter 2000000 -name SB9442-35 ${MSPATH}.
```

This paper has been typeset from a $\text{\TeX}/\text{\LaTeX}$ file prepared by the author.

APPENDIX B: WSCLEAN IMAGING COMMAND

We include the exact WSClean commands used to generate the reference reconstructions in our experiments. The parameters were chosen to ensure consistent spectral modelling and high imaging fidelity for both the simulated and ASKAP datasets. In simulated experiment, we used the following command

```
wsClean -join-channels -no-mf-weighting -fit-beam \
-fit-spectral-pol 5 -channel-range 0 36 \
-channels-out 36 -multiscale \
-scale ${PIXELSIZE}asec -niter 6000000 \
-nmiter 30 -weight briggs 0.0 -mgain 0.8 \
-size 512 512 -auto-threshold 0.4 \
-minuvw-m 0.001 -auto-mask 1 -mem 95 ${MSPATH}.
```

The pixel size in the command is calculated from the desired super-resolution factor. For the ASKAP data, the WSClean command is

```
wsClean -join-channels -gridder wgridder \
-size 4096 4096 -scale 2.2asec -minuvw-m 60 \
-no-mf-weighting -fit-spectral-pol 4 \
-channel-range 0 288 -channels-out 8 -mem 95 \
-weight briggs -0.25 -weighting-rank-filter 3 \
-reorder -clean-border 1 -multiscale \
```